

# 1 C-band radar data and in situ measurements for the monitoring of 2 wheat crops in a semi-arid area (center of Morocco)

3 Nadia Ouadi<sup>1,2</sup>, Jamal Ezzahar<sup>3,4</sup>, Saïd Khabba<sup>1,4</sup>, Salah Er-Raki<sup>4,5</sup>, Adnane Chakir<sup>1</sup>, Bouchra Ait  
4 Hssaine<sup>4</sup>, Valérie Le Dantec<sup>3</sup>, Zoubair Rafi<sup>1,2</sup>, Antoine Beaumont<sup>6</sup>, Mohamed Kasbani<sup>3</sup>, Lionel Jarlan<sup>3</sup>

5 <sup>1</sup>LMFE, Department of Physics, Faculty of Sciences Semlalia, Cadi Ayyad University, Marrakech, Morocco

6 <sup>2</sup>CESBIO, University of Toulouse, IRD/CNRS/UPS/CNES, Toulouse, France

7 <sup>3</sup>MISCOM, National School of Applied Sciences, Cadi Ayyad University, Safi, Morocco.

8 <sup>4</sup>CRSA, Mohammed VI Polytechnic University UM6P, Benguerir, Morocco.

9 <sup>5</sup>ProcEDE, Department of Applied Physics, Faculty of Sciences and Technologies, Cadi Ayyad University, Marrakech,  
10 Morocco.

11 <sup>6</sup>Atmo Hauts-de-France, Lille, France.

12 *Correspondence to:* J. Ezzahar (j.ezzahar@uca.ma)

13 **Abstract.** A better understanding of the hydrological functioning of irrigated crops using remote sensing observations is of  
14 prime importance in the semi-arid areas where the water resources are limited. Radar observations, available at high  
15 resolution and revisit time since the launch of Sentinel-1 in 2014, have shown great potential for the monitoring of the water  
16 content of the upper soil and of the canopy. In this paper, a complete set of data for radar signal analysis is shared to the  
17 scientific community for the first time to our knowledge. The data set is composed of Sentinel-1 products and *in situ*  
18 measurements of soil and vegetation variables collected during three agricultural seasons over drip-irrigated winter wheat in  
19 the Haouz plain in Morocco. The *in situ* data gathers soil measurements (time series of half-hourly surface soil moisture,  
20 surface roughness and agricultural practices) and vegetation measurements collected every week/two weeks including above-  
21 ground fresh and dry biomasses, vegetation water content based on destructive measurements, cover fraction, leaf area index  
22 and plant height. Radar data are the backscattering coefficient and the interferometric coherence derived from Sentinel-1  
23 GRDH (Ground Range Detected High resolution) and SLC (Single Look Complex) products, respectively. The normalized  
24 difference vegetation index derived from Sentinel-2 data based on Level-2A (surface reflectance and cloud mask)  
25 atmospheric effects-corrected products is also provided. This database, which is the first of its kind made available in open  
26 access, is described here comprehensively in order to help the scientific community to evaluate and to develop new or  
27 existing remote sensing algorithms for monitoring wheat canopy under semi-arid conditions. The data set is particularly  
28 relevant for the development of radar applications including surface soil moisture and vegetation parameters retrieval using  
29 either physically based or empirical approaches such as machine and deep learning algorithms.  
30 The database is archived in the DataSuds repository and is freely-accessible via the DOI: <https://doi.org/10.23708/8D6WQC>  
31 (Ouaadi et al., 2020a).

## 32 **1 Introduction**

33 The south-Mediterranean region has been identified as a hot spot of climate change (Giorgi, 2006; Giorgi and Lionello,  
34 2008; IPCC, 2014) that may worsen the water shortage already affecting the region. Up to 90% of available water is  
35 dedicated to irrigation (Ministre de l'agriculture et peche maritime du developement rurale et des eaux et forets, 2018).  
36 Indeed, the predicted temperature rise that could reach 3°C by 2050 combined to precipitation decrease and increased  
37 evapotranspiration could drastically increase the irrigation requirements. The demand for water is also already increasing in  
38 response to an ever-growing population and to changes of agricultural practices-intensification, conversion to cash crops,  
39 rise of irrigated areas (Ducrot et al., 2004; Fader et al., 2016; Jarlan et al., 2016). The monitoring of irrigated crops and the  
40 optimization of water use is therefore of prime importance for the sustainability of the water resources in the Mediterranean  
41 region. This requires the implementation of methods to monitor the crop water status and the underlying soil moisture (Wang  
42 et al., 2012).

43 Within this context, the observations from active spaceborne sensors in the microwave domain (radar) have shown great  
44 potential for the monitoring of crops (Mattia et al., 2003; Ouaadi et al., 2020b; Picard et al., 2003). The potential of radar  
45 data for monitoring irrigated crops originates from their high sensitivity to the water status of the surface including the water  
46 content of the above ground biomass and the moisture of the upper soil layer (Ulaby and Dobson, 1986). It is also sensitive  
47 to the structural properties of the observed target including the size and orientation of the canopy elements (leaves, stems,  
48 trunks) and the soil roughness. A key advantage of radar observations for monitoring crops, especially those crops growing  
49 during the rainy season such as wheat, is also that it is not prone to atmospheric perturbations. Sentinel-1 provides for the  
50 first time since 2014 backscattering coefficients at a resolution of 10 m and a revisit time of 6 days compatible with the high  
51 dynamic of annual crops at the field scale paving the way to an operational use of C-band radar data for crop monitoring.

52 Nevertheless, radar signal is a complex mix of backscattering from the soil and from the canopy that are often difficult to  
53 disentangle. The impact of any changes of the canopy structure such as the appearance of the heads during the heading stage  
54 of wheat (Brown et al., 2003; El Hajj et al., 2019; Ulaby et al., 1986) or of the soil roughness may also drastically impact the  
55 backscattering response. These processes are not fully understood and not always properly reproduced by the backscattering  
56 models.

57 The sensitivity of the backscattering coefficient to the surface soil moisture (SSM) is widely documented in the literature for  
58 bare or covered soils (Ezzahar et al., 2020; Ouaadi et al., 2020c, 2020b; Ulaby and Dobson, 1986; Zribi et al., 2014). Several  
59 retrieval approaches based on the inversion of a radiative transfer models (Bai et al., 2017; Gherboudj et al., 2011; El Hajj et  
60 al., 2016; Li and Wang, 2018; Ouaadi et al., 2020b) or based on linear or non-linear empirical regression (Gorrab et al.,  
61 2015; Ouaadi et al., 2020b) have been developed. The SSM derived from radar observations are also used to estimate RZSM  
62 (root zone soil moisture), a key variable in agronomy, through the combination with a land surface model (Cho et al., 2015;  
63 Das et al., 2008; Dumedah et al., 2015; Ford et al., 2014; Rodell et al., 2004; Sabater et al., 2006; Sure and Dikshit, 2019).

64 The presence of a canopy above the soil results in two more contributions to the backscattered signal: the volume scattering  
65 and the attenuated signal by the canopy. The water content of vegetation influences the dielectric properties, that in turn  
66 influence the radar backscatter from the vegetation (Ulaby et al., 1982). Based on these findings, some studies are focused on  
67 the retrieval of vegetation parameters from SAR (Synthetic Aperture Radar) data such as above-ground biomass (Hosseini  
68 and McNairn, 2017; Periasamy, 2018; Taconet et al., 1994) or even grain yield (Fieuzal et al., 2013; Patel et al., 2006). In  
69 addition to the backscattering coefficient, the polarization ratio and the interferometric coherence have demonstrated  
70 potentialities for the characterization of the vegetation including height (Blaes and Defourny, 2003; Engdahl et al., 2001),  
71 vegetation cover fraction (Wegmuller and Werner, 1997), fresh above-ground biomass (Mattia et al., 2003; Veloso et al.,  
72 2017), above-ground biomass (Ouaadi et al., 2020b) and vegetation water content (Ouaadi et al., 2020b). Other studies  
73 acknowledge the sensitivity of coherence to soil moisture (De Zan et al., 2014; Scott et al., 2017). Recent research suggests  
74 that radar observations could also provide valuable information on the canopy water status (Van Emmerik et al., 2015;  
75 Ouaadi et al., 2020d) for crop stress detection.

76 In situ measurements of vegetation and soil characteristics are always needed to improve our understanding of the radar  
77 response, to develop and calibrate radiative transfer models and to propose generic retrieval methods for the inversion of soil  
78 or vegetation variables. Nevertheless, in situ data set dedicated to these objectives are really specific in the sense that, for  
79 instance, soil roughness is only of interest for understanding the physical principle of observations in the microwave domain.  
80 Likewise, above-ground biomass is often measured by agronomist for crop modeling for instance but the partition between  
81 dry and wet matter, a key variable for radar acquisition, is hardly ever done. Indeed, the latter relies on heavy destructive  
82 measurements consisting in cutting all the vegetation elements within squares sample in the field and a double weighting  
83 before and after drying the samples in an oven. In this paper, a recent, multi-year and complete database composed of  
84 processed Sentinel-1 SAR data (the backscattering coefficient and the interferometric coherence), Sentinel-2 NDVI and  
85 measured variables on the soil, on the vegetation and on the agricultural practices are made available. The in situ data  
86 include automatic measurements as well as observations carried out during measurement campaigns once or twice every 15  
87 days throughout the growing season. This database covers 3 wheat seasons (2016-2017 to 2018-2019) of 3 different irrigated  
88 fields (Ouaadi et al., 2020b). It is a unique and valuable data set that can be used for vegetation and soil moisture monitoring  
89 applications including from radar observations. In addition, the multiyear database can be useful for multiyear time series  
90 analysis. In the next section, an overview of the field-location and a detailed description of the variables, including field  
91 measurements and remote sensing data processing, are presented. In Section 3, the variables are experimentally and  
92 physically analyzed to assess the consistency of the dataset. Conclusions are provided in Section 4.

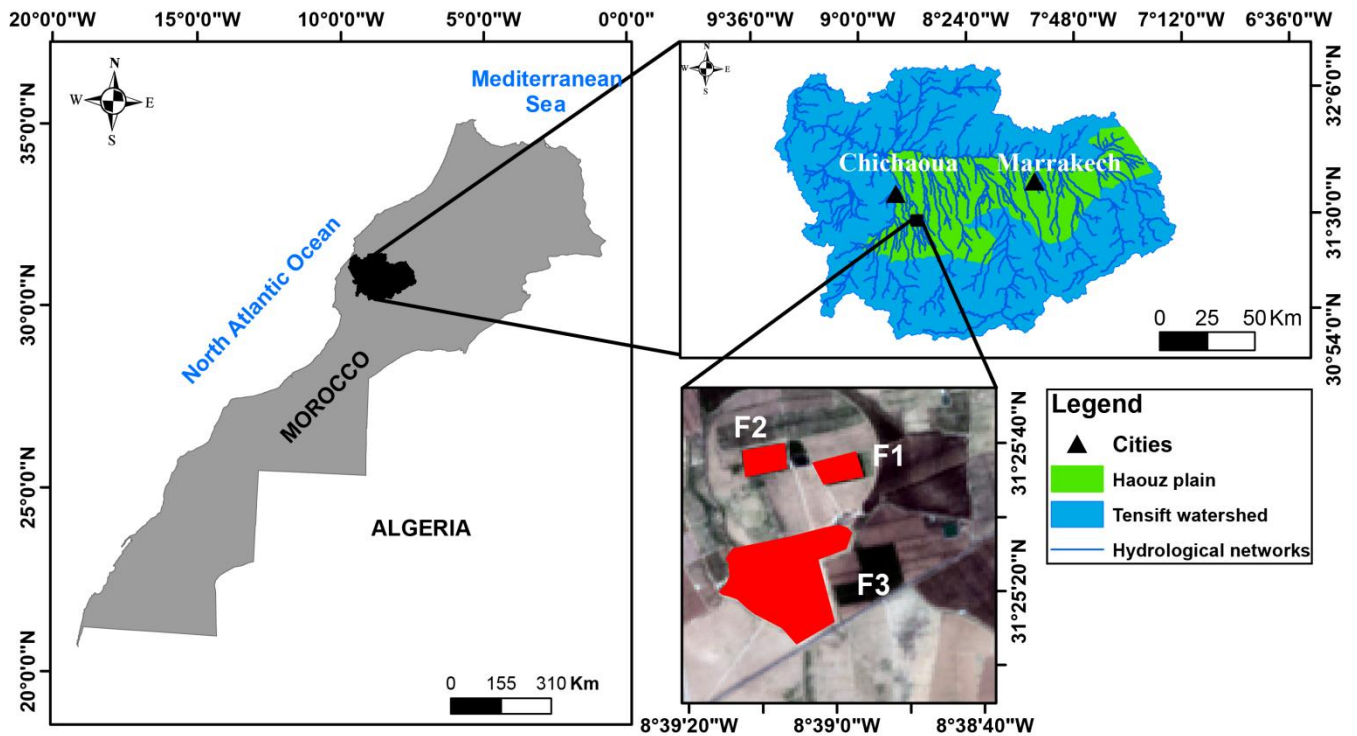
## 93 **2 Study area and experimental sites**

### 94 **2.1 Study area**

95 The database described in this paper is collected in the Haouz plain in the Tensift watershed, center of Morocco (Fig. 1).  
96 This plain is one of the most important plains in Morocco located at 550 m above sea level and covers about 6000 km<sup>2</sup> of  
97 which 2000 km<sup>2</sup> are irrigated. The climate in the region is Mediterranean semi-arid, with an annual average precipitation of  
98 about 250 mm. The distribution of precipitations highlights a wet season with around 85% of annual precipitations between  
99 October and April, and a dry season from May to September. The maximum average of temperature occurs during summer  
100 in July-August (about 35°C) and the minimum in January (about 5°C) (Abourida et al., 2008). The average air humidity is  
101 about 50% and the reference evapotranspiration ET<sub>0</sub> is around 1600 mm/year (Jarlan et al., 2015), which is greatly  
102 exceeding the annual rainfall. The agricultural production in the plain is not very diverse, focusing on cereals (51% of the  
103 irrigated areas), olive trees (30% of the irrigated area), 9% of fodder production and 2% of market gardening for cattle  
104 breeding while the non-irrigated part of the plain is cropped with rainfed wheat (Abourida et al., 2008). Wheat is usually  
105 sown between November and January depending on precipitation distribution, even for irrigated field, and on cultivar.  
106 Harvest usually occurs in May or June.

### 107 **2.2 Experimental sites**

108 The database concerns three irrigated fields (F1, F2 and F3) located within a private farm in the province of Chichaoua  
109 located 65 Km west of Marrakech city (Fig. 1). F1 and F2 are monitored during two successive growing seasons (2016-2017  
110 and 2017-2018) while F3 is monitored during the season 2018-2019. The fields are sown using an automatic seed drill. They  
111 are irrigated using the drip technique. For all the fields, the wheat is cropped once a year during winter-spring (see Table 1  
112 for sowing and harvest dates). After harvest, the fields are generally used for cattle grazing until mid-July when the plowing  
113 works started. Table 1 summarizes some general information about the fields. Please note that during the 2017-2018 season,  
114 wheat in F2 is affected by specific growing conditions: i) the development of adventices belonging to the wild thistles family  
115 characterized by a horizontal structure, ii) the seeding density is higher than in F1, and iii) the seeding is a mixture of barley  
116 and wheat within F2. This resulted in very long stems: 146 cm in F2 compared to 110 cm in F1 in April 2018. Finally, these  
117 long stems in F2 are laid down by the wind from April 12, 2018. A picture of F2 during 2017-2018 is provided in appendix  
118 A (Fig. A1). Although such exceptional growing conditions are not very likely, it has been chosen to include this crop season  
119 in the data set to cover different conditions of growth.



121  
 122 **Figure 1.** Location of the study fields: F1, F2 and F3 are drip-irrigated wheat plots in a private farm (“Domaine Raffi”) near  
 123 Chichaoua city in the Haouz plain, center of Morocco.

124 **Table 1.** General information about the three fields

Field	Area (ha)	Season	Sowing date	Harvest date	Irrigation	Sand (%)	Clay(%)
F1	1.5	2016-2017 &	Nov 25, 2016	May 16, 2017	Drip technique	32.5	37.5
F2	1.5	2017-2018	Nov 27, 2017	June 08, 2018			
F3	12	2018-2019	Nov 04, 2018	June 06, 2019			

## 125 3 Database

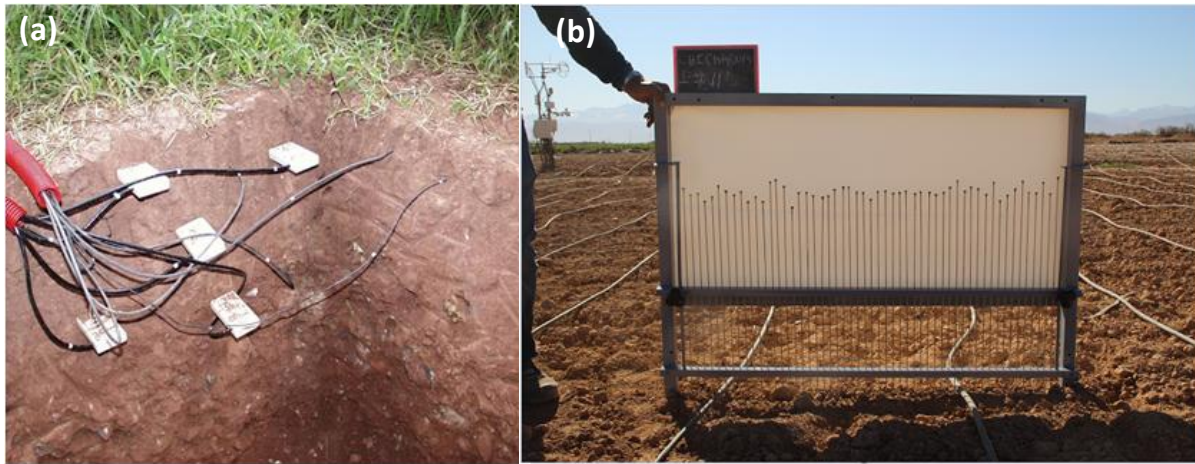
### 126 3.1 Field datasets

127 The field datasets consist of automatic measurements of soil moisture and weather data in addition to punctual surveys for  
 128 surface roughness, biomass, vegetation water content, canopy height, green leaf area index and cover fraction. Table A1 in

129 the appendix summarizes the details of the 26, 18 and 16 field campaigns carried out during 2016-2017, 2017-2018 and  
130 2018-2019 seasons, respectively.

### 131 3.1.1 Soil moisture

132 SSM is automatically measured every 30 min using Time Domain Reflectometry sensors (TDR), (Campbell Scientific  
133 CS616) using two sensors buried at a depth of 5 cm: one under the drippers and another one between. The average is  
134 computed in order to get a representative SSM value of the field. In addition, similar sensors are buried for RZSM measuring  
135 at 25 and 35 cm of depth over F1 and F3 while one sensor is buried at 30 cm over F2 by lack of additional sensor. Figure 2a  
136 illustrates an example of TDR sensors at different depths.



137

138 **Figure 2. Examples of (a) TDR sensors installed at different depths and b) a pin profiler picture taken over one of the ploughed**  
139 **field with drip irrigation tubes installed.**

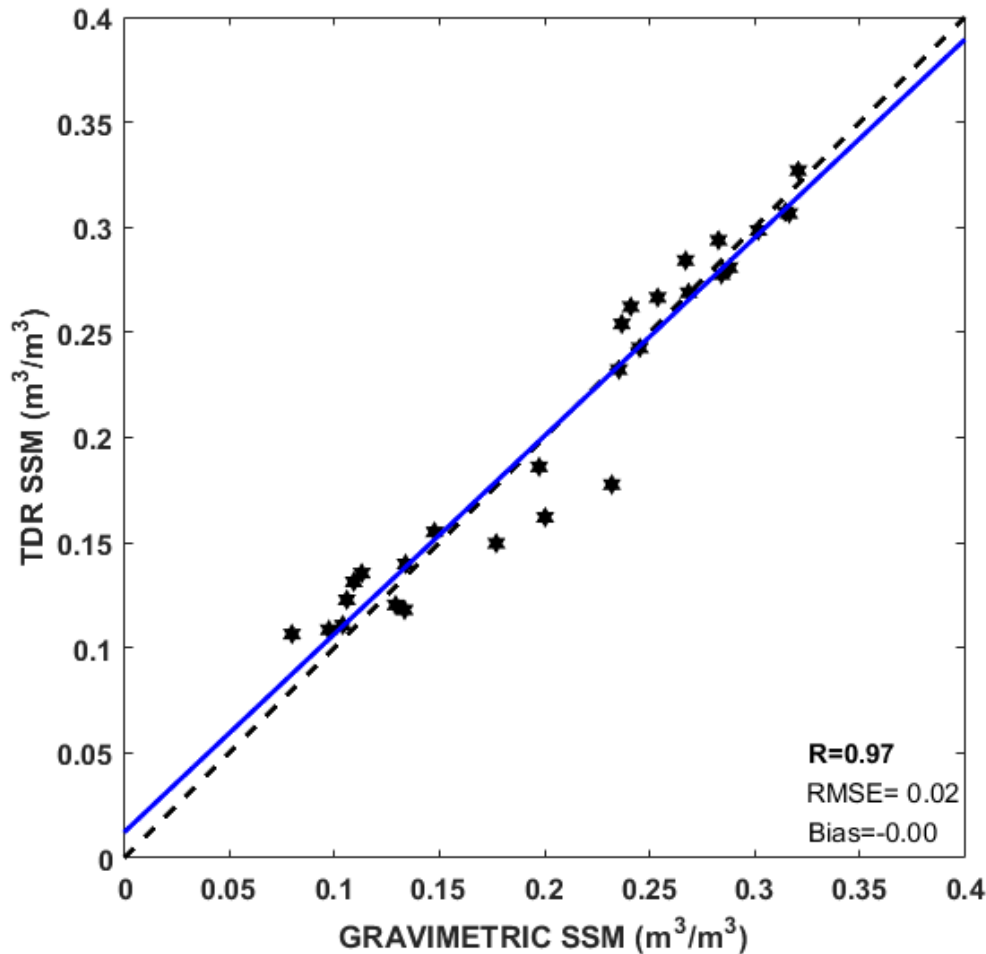
140 TDR sensors are calibrated using the gravimetric technique. The calibration is done during 2016-2017 season using samples  
141 taken from the first 5 cm from both fields F1 and F2 and then the calibrated equation is applied to F1, F2 and F3 data as the  
142 soil characteristics are similar and the same sensors are used. For that purpose, an aluminum core of 392.5 cm<sup>3</sup> is used to  
143 collect samples at the TDR installation depths. Three samples are collected per day and per field during five days chosen  
144 with different soil moisture conditions in order to cover a wide range of values (0.08 to 0.33 m<sup>3</sup>/m<sup>3</sup>). A linear regression is  
145 established between the volumetric water content and the square root of the TDR time response (named  $\tau$  in second) as  
146 follow:

147

$$SSM = a_{TDR} * \sqrt{\tau} + b_{TDR} \quad (1)$$

148 The calibrated values using data of both fields are  $a_{TDR} = 0.275 \text{ m}^3/\text{m}^3/\text{s}^{0.5}$  and  $b_{TDR} = -1.154 \text{ m}^3/\text{m}^3$ . Figure 3  
149 illustrates the calibration results with all the samples displayed. The statistical metrics are: correlation coefficient  $R = 0.97$ ,  
150 Root Mean Square Error  $RMSE = 0.018 \text{ m}^3/\text{m}^3$  and no Bias. When considering both fields separately, the results for (F1, F2)  
151 are  $R = (0.90, 0.94)$ ,  $RMSE = (0.023, 0.01) \text{ m}^3/\text{m}^3$  and  $Bias = (-0.002, 0.003) \text{ m}^3/\text{m}^3$ .

152 The calibrated equation is also applied for the RZSMs assuming that the soil properties are the same at different depths.  
153 Figure A2 in appendix A illustrates an example of an RZSM time series over F1.



154

155 **Figure 3. Surface soil moisture measured by TDR versus gravimetric measurements using samples collected over both fields F1**  
156 **and F2 during 2016-2017 growing season. The blue solid line is the linear regression and the dashed line is Y=X.**

### 157 3.1.2 Surface roughness

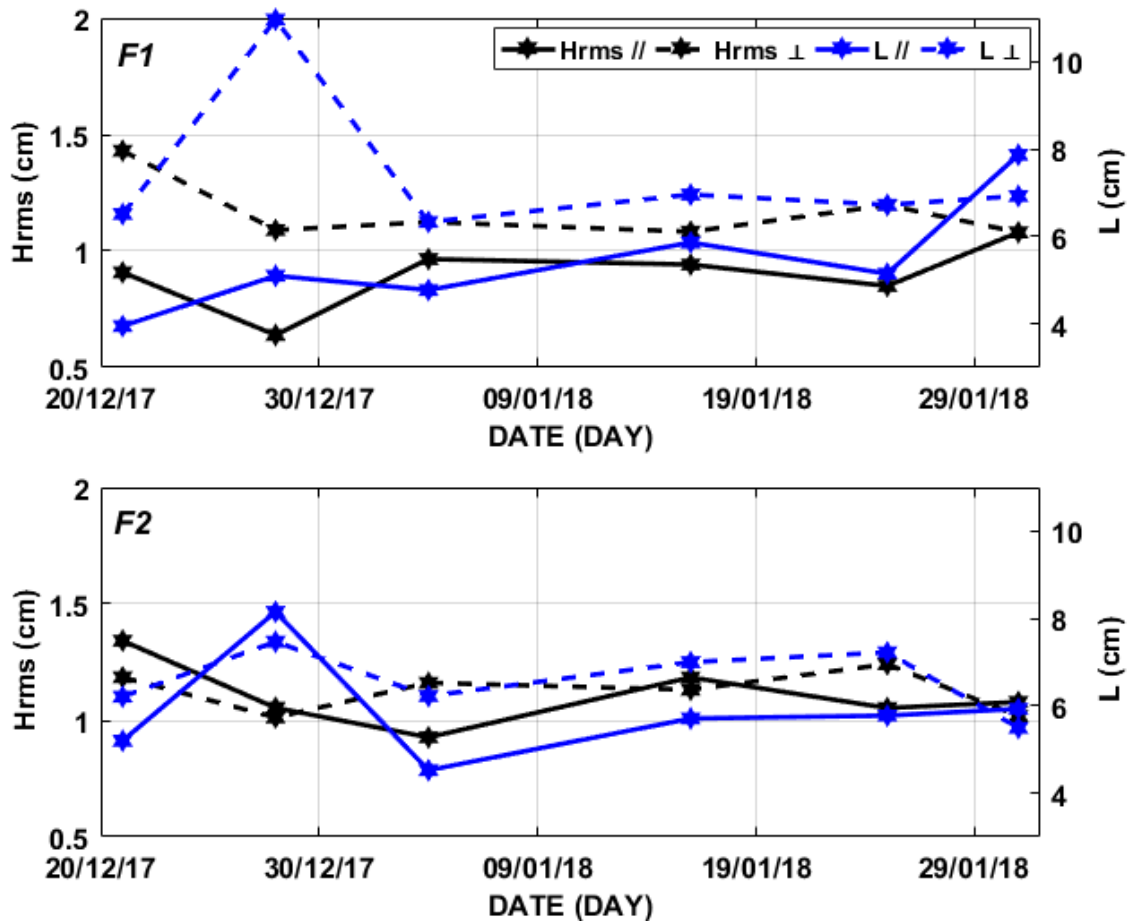
158 Surface roughness characterizes the micro variation of the ground surface elevation within a given area/field (Allmaras et al.,  
159 1966). It affects particularly the SAR signal and to a lesser extent the visible and near infrared (Girard and Girard, 1989).  
160 The two parameters that characterize the surface roughness are the root mean square height ( $h_{rms}$ ) and the correlation length  
161 ( $L$ ).  $h_{rms}$  provides a vertical descriptor of ground roughness by measuring the elevation of the surface along one or more  
162 observation lines and calculating the standard deviation of the recorded values. The second parameter ( $L$ ) corresponds to the  
163 distance between measurements from which the heights between points are statistically independent. This parameter

164 provides a horizontal description of the ground surface roughness, more specifically the organizational structure and spatial  
 165 continuity of the microtopography (Nolin et al., 2005). Over the 3 studied fields, measurements of the surface roughness are  
 166 taken during the first stage of wheat (from emergence to early tillering) when the ground is not totally covered by the  
 167 canopy. We used a pin profiler of 1 m length, composed of a set of 53 metal needles of equal length every 2 cm (Fig. 2b). 16  
 168 sample pictures are taken per field and per date including eight pictures parallel and eight pictures perpendicular to the rows  
 169 direction. The pictures are taken using Canon 6EOS 600D equipped with TAMRON lens (Model A14).  
 170 The images are processed in MATLAB based on the detection of the top position of each needle.  $h_{rms}$  and L are computed  
 171 from the auto-correlation function and then the average per direction, per field and per date is computed. For illustration, Fig.  
 172 4 shows the time series of  $h_{rms}$  and L parameters computed separately for each direction for F1 and F2 during the season  
 173 2017-2018 while the average value per season are summarized in Table 2 for F1, F2 and F3.

174 **Table 2. Average values of the roughness parameters (8 samples are gathered per field and per direction).**

		F1		F2		F3	
		$h_{rms}$ (cm)	L (cm)	$h_{rms}$ (cm)	L (cm)	$h_{rms}$ (cm)	L (cm)
<b>2016-2017</b>	Parallel	0.92	5.02	1.19	5.77		
	Perpendicular	1.34	5.88	1.19	5.8		
	Average	1.13	5.45	1.19	5.78		
<b>2017-2018</b>	Parallel	0.89	5.44	1.1	5.88		
	Perpendicular	1.16	7.4	1.12	6.6		
	Average	1.02	6.42	1.11	6.24		
<b>2018-2019</b>	Parallel					0.83	6.54
	Perpendicular					0.96	7.32
	Average					0.89	6.93

175  
 176 Based on the range of  $h_{rms}$  measurements ( $0.83 < h_{rms} < 1.35$ ), it can be clearly seen that the fields are characterized by a  
 177 slightly rough or smooth surface, which is the general case of disk tilling fields. After sowing, a slight change is observed at  
 178 the start of the crop season (December 28, 2017, see Fig. 4). At that time, the soil has just been prepared for sowing and rows  
 179 are directly exposed to rain. The fact that the rows are still visible in the field also explains the differences observed between  
 180 both directions early in the season. This anisotropy disappeared quickly with irrigation, rainfall and plant growth.  $h_{rms}$  and L  
 181 are almost constant from early January onwards. Indeed, it has been shown that after sowing, roughness is affected by very  
 182 limited temporal variations (Bousbih et al., 2017) as no soil works occur after sowing. It is usually kept constant during the  
 183 crop season (El Hajj et al., 2016; Gherboudj et al., 2011; Gorraab et al., 2015; Ouaadi et al., 2020).



184

185 **Figure 4. Time series of  $h_{rms}$  and  $L$  computed from parallel and perpendicular measurements separately for F1 and F2 during the**  
 186 **season 2017-2018.**

187 **3.1.3 Biomass and water content**

188 Biomass and water content are two biophysical parameters of crucial importance in different agricultural applications  
 189 including particularly plant stress monitoring, radar backscattering response, crop yield and evapotranspiration modeling.  
 190 Within each field, eight samples are collected once a week/two weeks during the growing season. The samples are chosen  
 191 randomly so that the average is representative of the plot. A quadrates of an area of  $0.0625 \text{ m}^2$  is used for the sampling (Fig.  
 192 5). The samples are weighed first in the field to get fresh above-ground biomass (FAGB). The corresponding above ground  
 193 biomass (AGB) expressed in kg of dry matter by  $\text{m}^2$  is determined at the laboratory by drying the samples in an electric oven  
 194 at  $105^\circ\text{C}$  for 48 hours. The vegetation water content (VWC) is thus computed as the difference between FAGB and AGB  
 195 (Gherboudj et al., 2011).

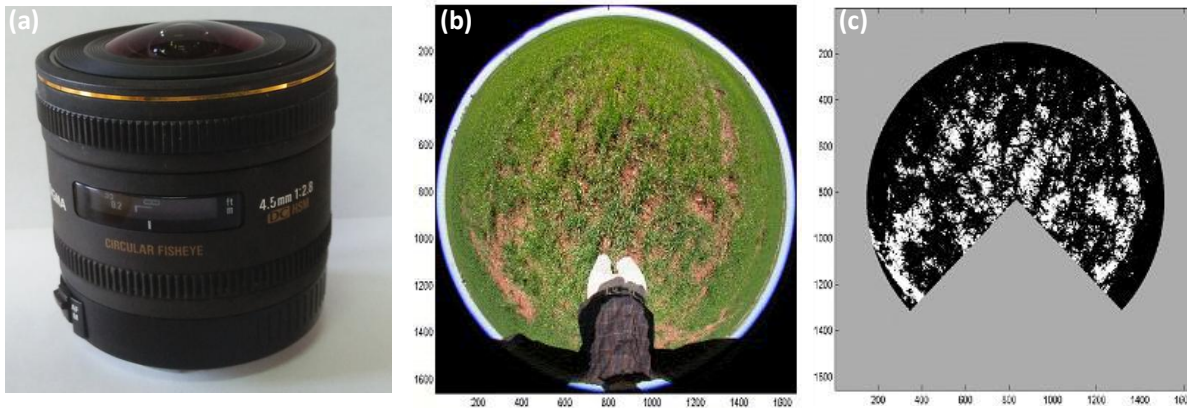


196

197 **Figure 5. Photo taken during a measurement campaign illustrating a sample of above-ground biomass measurement.**

#### 198 **3.1.4 Canopy height, green leaf area index and cover fraction**

199 Canopy height ( $H$ ), green leaf area index ( $GLAI$ ) and cover fraction ( $F_C$ ) are measured every week during the growing  
200 season. Values from eleven different places are averaged and considered as a representative measure of the field.  $H$  is simply  
201 measured using a measuring tape while  $GLAI$  and  $F_C$  are computed by processing hemispherical photos (Fig. 6b) using  
202 MATLAB software following the method described in Duchemin et al. (2006) and Khabba et al. (2009). The eight photos  
203 per date and per field are taken using a camera Canon 6EOS 600D with SIGMA 4.5 mm F2.8 EXDC circular fisheye HSM  
204 (Fig. 6a). Photos are taken in optimal lighting conditions to avoid shadow effects and over-exposure phenomena which make  
205 classification more difficult. The algorithm is based on the binarization of the hemispherical images by thresholding a  
206 greenness index. Next, the useful part of the images is extracted by masking the operator and the high viewing angles ( $> 75^\circ$ )  
207 (Fig. 6c). Finally, the ground-covered area is extracted on concentric rings associated with fixed viewing angles and the  
208 average of all pictures is the field  $GLAI$ . Using the same process,  $F_C$  is calculated as the ratio of the vegetation pixels number  
209 to the pixels total number.



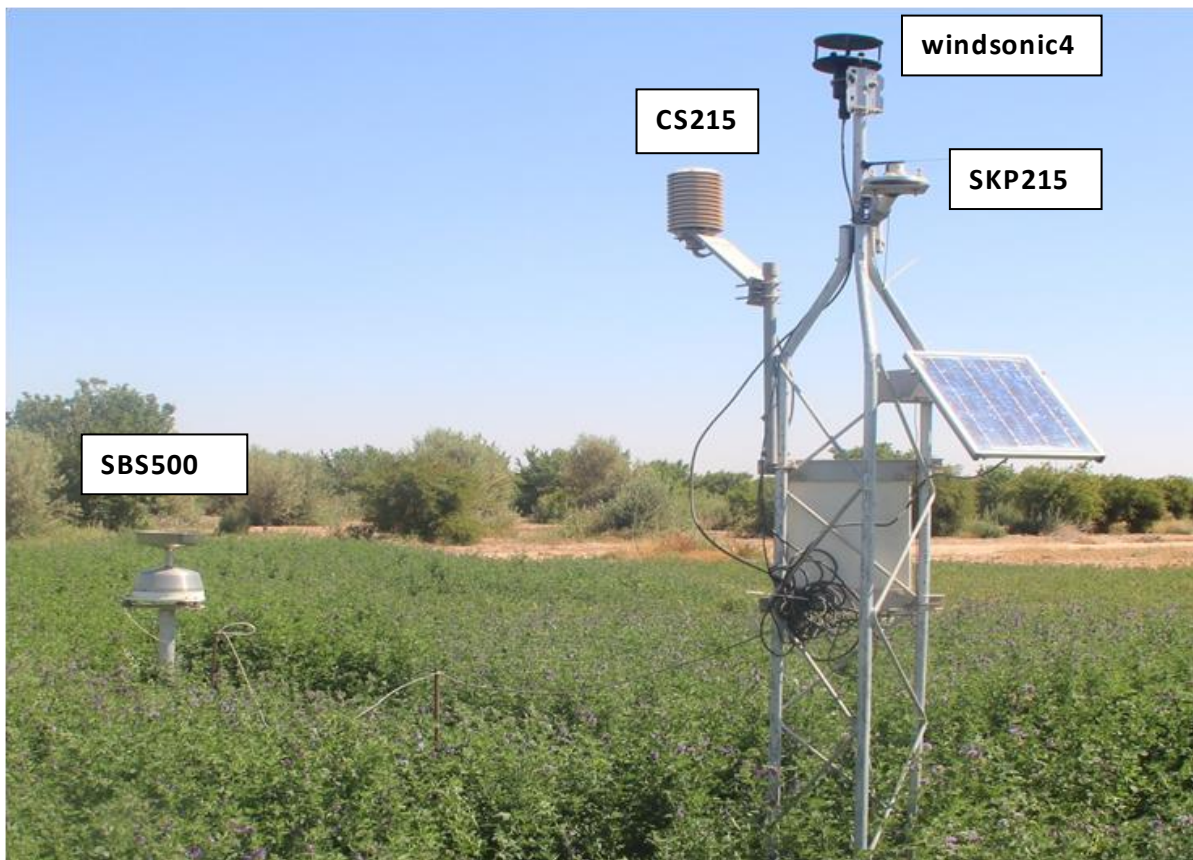
210

211 **Figure 6. (a) the 4.5 mm F2.8 EXDC circular fisheye HSM, (b) hemispherical photo and (c) result of the processing after**  
 212 **binarization and after masking the operator and the high viewing angles ( $> 75^\circ$ ).**

### 213 3.1.5 Irrigation and weather data

214 F1, F2 and F3 are irrigated using the drip technique. Irrigation quantities are determined by the farmer by estimating the  
 215 daily evapotranspiration under standard conditions ( $ET_c$ ) in the region computed using the FAO-56 model simple approach  
 216 (Allen et al., 1998). The cumulative  $ET_c$  for a given period (usually one week) is applied during one or more events per week  
 217 depending on the farmer's constraints (e.g. availability of workforce) and on the weather conditions (e.g. occurrence of rain).  
 218 The irrigation pipes are spaced by 0.7 m while the distance between the drippers along the pipe is 0.4 m. Over F1 and F2, the  
 219 flowrate of each dripper is 7.14 mm/hour. The irrigation takes place about 105 min (12.53 mm). A flowmeter mounted  
 220 downstream of a valve allowed an accurate collection of irrigation volumes. F2 and F3 are irrigated according to FAO  
 221 recommendations while F1 is stressed voluntarily. The stress involved in F1 is during the first season (2016-2017) only. By  
 222 contrast, the 2017-2018 season was wet so that there is no clear stress observed on the field. The irrigation dates and  
 223 amounts over F1 and F2 during both seasons are made available throughout this database while irrigation over F3 are not  
 224 available.

225 The weather data including precipitation, air temperature, relative humidity, solar radiation, wind speed and direction are  
 226 collected by an automatic weather station installed over an alfalfa field near the studied fields (Fig. 7). The weather station  
 227 provides continuously meteorological data every 30 min. The sensor Campbell CS215 is used to measure the air temperature  
 228 and the relative humidity (Fig. 7). The global solar radiation and the wind direction and speed are measured using Campbell  
 229 SKP215 and Campbell windsonic4, respectively. The precipitation are measured using the Rain Gauge (Campbell SBS500)  
 230 shown in Fig. 7.



231  
 232 **Figure 7. Automatic weather station installed over an alfalfa field near F1, F2 and F3.**

233 **3.2 Remote sensing datasets**

234 **3.2.1 Sentinel-1**

235 Sentinel S1A and S1B are earth observation satellites developed for the Copernicus initiative and launched by the European  
 236 Space Agency on April 2014 and 2016, respectively. During full operation, S1A and S1B are maintained in the Near-polar  
 237 Sun-synchronous orbit at 693 km altitude, phased 180°, providing a revisit time of six days (Torres et al., 2012). S1 is a  
 238 synthetic aperture radar operating at C-band with a frequency of 5.33 GHz, mapping the entire world in 175 orbits per cycle.  
 239 The main operational imaging mode is the Interferometric Wide-swath mode (IW). IW acquires data with a wide swath of  
 240 250 km with high geometric (azimuth resolution 20 m and ground range resolution 5 m) and radiometric resolution (Mission  
 241 and Services, 2012). IW mode supports operation in single and dual polarization (HH, VV, HH/HV and VV/VH) and covers  
 242 a range of incidence angles between 31° and 46°. The product is composed of three Sub-Swath acquired in TOPSAR  
 243 imaging technique which significantly reduces the scalloping effect (Zan and Guarnieri, 2006).

244 Level 1 products are systematically processed and available within 24 hours, free of charge from the Sentinel-1 Data Hub  
 245 website (<https://scihub.copernicus.eu>). The website provides data under two types of products: GRDH (Ground Range  
 246 Detected High resolution) and SLC (Single Look Complex).

247 In this database, 561 GRDH and SLC products are processed (Table 3). Among them, 124 images are acquired over F3  
 248 during 2018-2019 growing season and 437 over F1 and F2 from October 01, 2016, to July 31, 2018, along the ascending  
 249 #118 (221 images) and descending #52 (216 images) relative orbits. This period includes two agricultural seasons in addition  
 250 to the summer period.

251 **Table 3. Characteristics of the sentinel-1 products processed over the three fields for the monitored periods**

Field	Season	Relative Orbit Number	Incidence angle	Relative Orbit	Overpass time	Product	Number of images
<b>F1 and F2</b>	October 2016 - July 2018	118	45,6°	Ascending	18:30	GRDH	112
						SLC	109
		52	35,2°	Descending	06:30	GRDH	110
						SLC	106
<b>F3</b>	November 2018 - May 2019	118	45,6°	Ascending	18:30	GRDH	32
						SLC	31
		52	35,2°	Descending	06:30	GRDH	31
						SLC	30

252 ***Backscattering coefficient***

253 GRDH products are provided by ESA with a square pixel size and contains only the intensity information. The  
 254 backscattering coefficients are extracted using the OrfeoToolbox (CNES, 2018). The processing procedure consists of three  
 255 steps (Frison and Lardeux, 2018) :

- 256 1. *Thermal noise removal*: SAR product contains not only the useful signal but also the unwanted noise disturbing the  
 257 information contained in the intensity images, especially when the backscattered power is low. The thermal noise is  
 258 an additive noise. The compensation of this noise can be performed by subtracting the scaled noise power using the  
 259 calibrated noise vectors provided by ESA.
- 260 2. *Calibration*: The "calibration" step aims to convert the digital accounts into a physically interpreted parameter: the  
 261 backscattering coefficient. A calibration vector included in the GRDH products contains the necessary information  
 262 to convert the digital values to the backscattering coefficient.
- 263 3. *Terrain correction*: S1-SAR data are sensed with viewing angle greater than zero which induces distortion in the  
 264 products because of the lateral viewing geometry. The "Terrain corrections" module is used to compensate these  
 265 distortions and get as much possible images with the real geometric representation. The images are projected on the

266 Earth's surface using a Digital Elevation Model (DTM). The DTM SRTM (Shuttle Radar Topography Mission) of  
 267 30 m of resolution is used according to the method described in Small and Schubert (2008).  
 268 SAR images are affected by the speckle noise, which is mainly due to the relative phase of individual scatters within a  
 269 resolution cell. Many filters have been developed to remove the speckle noise although the best filter is the spatial average.  
 270 The presented database is generated using a simple average per field of 120, 121 and 1100 pixels for F1, F2 and F3,  
 271 respectively with a mean standard deviation of around 1.55 dB. In order to visualise data dynamics, backscattering  
 272 coefficients are converted into dB.

### 273 *Interferometric coherence*

274 Sentinel-1 SLC products are provided in slant-range geometry. It contains three sub-swath images IW1, IW2 and IW3. Each  
 275 sub-swath is composed by nine bursts with black-fill demarcation. By contrast with GRD, both intensity and phase  
 276 information are kept. The phase information is used for the computation of interferometric coherence. SAR interferometry  
 277 consists of correlating two images acquired from two positions in space slightly separated from each other (with two radars  
 278 mounted on the same platform) or at different times by exploiting repeated orbits of the same satellite such as for Sentinel-1.  
 279 Thanks to its high temporal resolution (six days per orbit), the interferometric coherence is computed from two consecutive  
 280 acquisitions of the same orbit.

281 The interferometric coherence, given by the Eq. (2), for a local neighborhood of N pixels, is generated by cross multiplying,  
 282 pixel by pixel, the first SAR image  $z_i$  with the complex conjugate  $z_i^*$  of the second (Bamler and Hartl, 1998; Touzi et al.,  
 283 1999).

284

$$285 \quad \rho = \frac{\sum_{i=1}^N z_i \cdot z_i^*}{\sqrt{\sum_{i=1}^N |z_i|^2 \cdot \sum_{i=1}^N |z_i'|^2}} \quad (2)$$

286 The interferometric coherence  $|\rho|$  varies between zero (incoherence) and one (perfect coherence). The interferometric  
 287 coherence is related to the movements of the scatterers within a given canopy. It decreases (loss of coherence) in the case of  
 288 dense vegetation while high values are obtained over bare soils. Loss of coherence could be caused by temporal interval  
 289 between acquisitions, orbit errors, vegetation development/movement or processing errors. The random dislocation of  
 290 scatters because of the weather (wind and rain) or the plants growth is the main cause of the temporal decorrelation.

291 Sentinel application platform SNAP is used to compute the interferometric coherence from S1-SLC products in five steps  
 292 (Veci, 2015):

- 293 1. *Apply-Orbit-file*: This module is applied for a better estimation of the position and speed of the satellite using the  
 294 orbit state vector. Preliminary, a predicted orbit state vector is contained in the metadata but it is not accurate. The  
 295 precise orbit is made available one month after data acquisition at the later. For this reason, the automatic download  
 296 in SNAP is used in order to update the orbit state vectors.

- 297 2. *Back-geocoding*: The two images need to be co-registered. One of the images is the master and the other is the  
298 slave. This step ensures that each pixel of the slave image is aligned with the corresponding pixel in the master  
299 image so that both pixels contain contributions from the same target. The DEM is required for "*Back-geocoding*"  
300 step, SNAP allows either to enter it manually or to download it automatically.
- 301 3. *Coherence*: This module in SNAP allows the computation of the interferometric coherence between the two images  
302 for a given local neighborhood. In order to get a square pixel of 13.95 m, azimuth\* range are fixed to 3\*15 in the  
303 processing.
- 304 4. *TOPSAR-Deburst*: The black-fills in between bursts are deleted separately for both polarization images (VV and  
305 VH).
- 306 5. *Terrain-Correction*: Finally, the processed images are projected on the earth surface using a DEM.

### 307 3.2.2 Sentinel-2 NDVI

308 Sentinel-2 optical satellites S2A and S2B are launched by ESA in June 2015 and March 2017, respectively. They are placed  
309 in opposition on the same orbit at an altitude of 800 km. Sentinel-2 provides data every 5 days with a width of 290 km and a  
310 resolution of 10 to 60 m according to spectral bands (13 bands) ranging from visible to the medium infrared. The National  
311 Centre for Space Studies (CNES) provides Level-2A products atmospherically corrected free of charge via the PEPS  
312 platform (<https://peps.cnes.fr/>) or the Theia website (<https://theia.cnes.fr/>). Data are corrected from atmospheric effects by  
313 the Center for the Study of the Biosphere from Space (CESBIO) using the MAJA chain (Hagolle et al., 2015). The  
314 atmospheric corrections are performed in three steps:

- 315 1. The satellite top-of-atmosphere (TOA) reflectances are corrected from the absorption by the atmospheric gas  
316 molecules using the absorption part of the Simplified Model for Atmospheric Correction (SMAC) method by  
317 Rahman et al., 1994. The concentrations of the ozone, the oxygen and the water vapor are obtained from satellite  
318 data (ozone) and meteorological data (water vapor, pressure).
- 319 2. The detection of the clouds (and cloud's shadows) is based on the multi-temporal cloud detection method proposed  
320 by Hagolle et al., 2010 .
- 321 3. The estimation of the aerosol optical thickness (AOT) relies on a hybrid method merging the criteria of a multi-  
322 spectral method with the multi-temporal technique developed initially for the VEN $\mu$ S satellite mission by Hagolle  
323 et al., 2010. The AOT is used along with the surface altitude, the viewing geometry and the wavelength in the  
324 parameterization of look-up tables for the conversion of TOA reflectances already corrected in step "1" into surface  
325 reflectances. The look-up tables are provided by the successive orders of scattering code (Lenobel et al., 2007) used  
326 in the modeling of molecular and aerosol scattering effects. A different look-up table is computed for each aerosol  
327 model.

328 Data are downloaded from the Theia site. Among the available products, only the products non-covered with clouds are used  
329 corresponding to ten, twenty-five and twenty-six images for 2016-2017, 2017-2018 and 2018-2019 agricultural seasons,  
330 respectively. Please note that during the season 2016-2017, only S2A was in the orbit which explains the limited number of  
331 images (10). Next, the Normalized Difference Vegetation Index (NDVI) corresponding to each pixel is computed from band  
332 4 and 8. An average per field is used to compute the time series of each field.

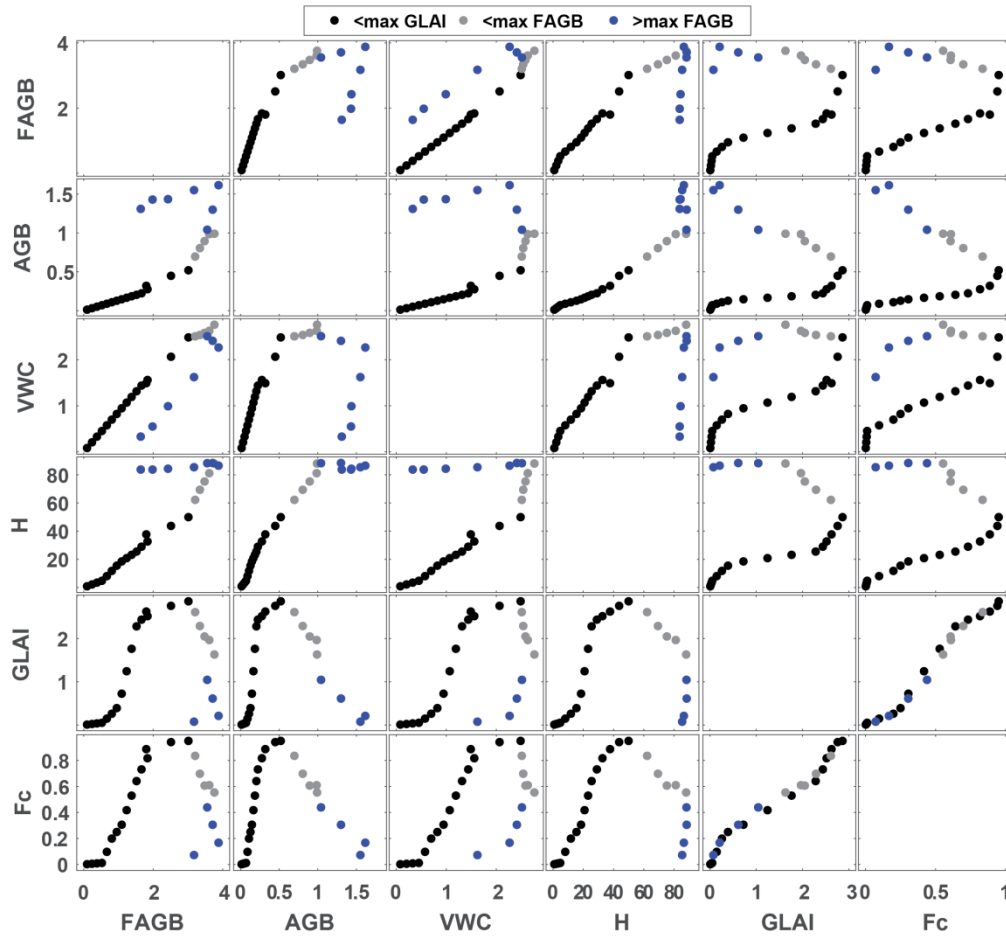
## 333 4 Data analysis

### 334 4.1 Vegetation variables

335 In this section, the relationships between the different variables (GLAI, FAGB, AGB, VWC and H) that characterize the  
336 vegetation growth and development are firstly investigated. These relationships are extensively used for different  
337 applications such as the calibration of backscattering models and the development of retrieval approaches (Chauhan et al.,  
338 2018). Several land surface or crop model relies on empirical relationships to predict Fc or H as well (Bigéard et al., 2017;  
339 Castelli et al., 2018). Other agricultural models compute AGB from GLAI using linear or polynomial relationships (Major et  
340 al., 1986; Petcu et al., 2003). Figure 8 displays the resulting relationships using data from F1 by selecting only the 2016-  
341 2017 season for illustration purposes. These relationships are computed separately based on the data recorded before and  
342 after the peaks of GLAI and FAGB.

343 The nature of the relationship changes depending on the structure (biomass variables) or on the greenness of the plant  
344 (GLAI). The biomass variables (FAGB, AGB and VWC) and H increase up to the biomass peak. Afterwards, a reverse  
345 evolution can be observed characterized in particular, by a decorrelation between FAGB/VWC and AGB. This is mainly  
346 related to the senescence process of the vegetation; the leaves begin to dry progressively with the start of the grain filling, so  
347 that the Sapflow (water, carbohydrates, proteins and mineral salts) migrates to the heads at the top of the plant (Farineau and  
348 Morot-Gaudry, 2018). Indeed, VWC and AGB are highly correlated until vegetation peak (the correlation coefficient  $R =$   
349  $0.94$  before the peak and  $R = -0.20$  afterwards) while FAGB being dominated by the plant water content is highly correlated  
350 with VWC during the whole crop season ( $R=0.99$  before the peak and  $R = 0.98$  afterwards). Likewise, H is highly correlated  
351 to FAGB, VWC and AGB until vegetation peak ( $R > 0.97$ ) when H remains at its maximum value while AGB continue to  
352 increase with grain filling and VWC and FAGB decrease because of the vegetation drying. The relationship of these  
353 variables (FAGB, AGB, VWC and H) with GLAI and Fc is quite different. The curves are of a parabolic shape with a  
354 maximum reached around the GLAI peak. A timing shift between the peaks of GLAI and FAGB is observed. This is  
355 probably related to the senescence of the lower leaves, which leads to an earlier drop of GLAI than of FAGB. Between the  
356 peaks of GLAI and FAGB, GLAI decreases while i) AGB and H increase and ii) FAGB increases slightly while VWC is  
357 almost constant. After the FAGB peak, AGB goes on increasing due to grain filling while the VWC decreases due to drying  
358 of the plant. FAGB which is the sum of AGB and VWC is almost constant.

Vegetation parameters over F1, 2016 - 2017 season



359

360 **Figure 8. Scatterplots of the relationships between wheat measured variables: FAGB, AGB, VWC, H, GLAI and Fc. Data are**  
 361 **presented separately using the maximum of GLAI and FAGB as thresholds: data <max GLAI are in black, data < max FAGB**  
 362 **(and > max GLAI) are in grey and data > max FAGB (and > max GLAI) are in blue.**

363 **4.2 Radar data**

364 The time series of the backscattering coefficient, the polarization ratio and the interferometric coherence are analyzed here  
 365 for two agricultural seasons and a summer period on F1 and F2 and at two incidence angles (35.2° and 45.6°).

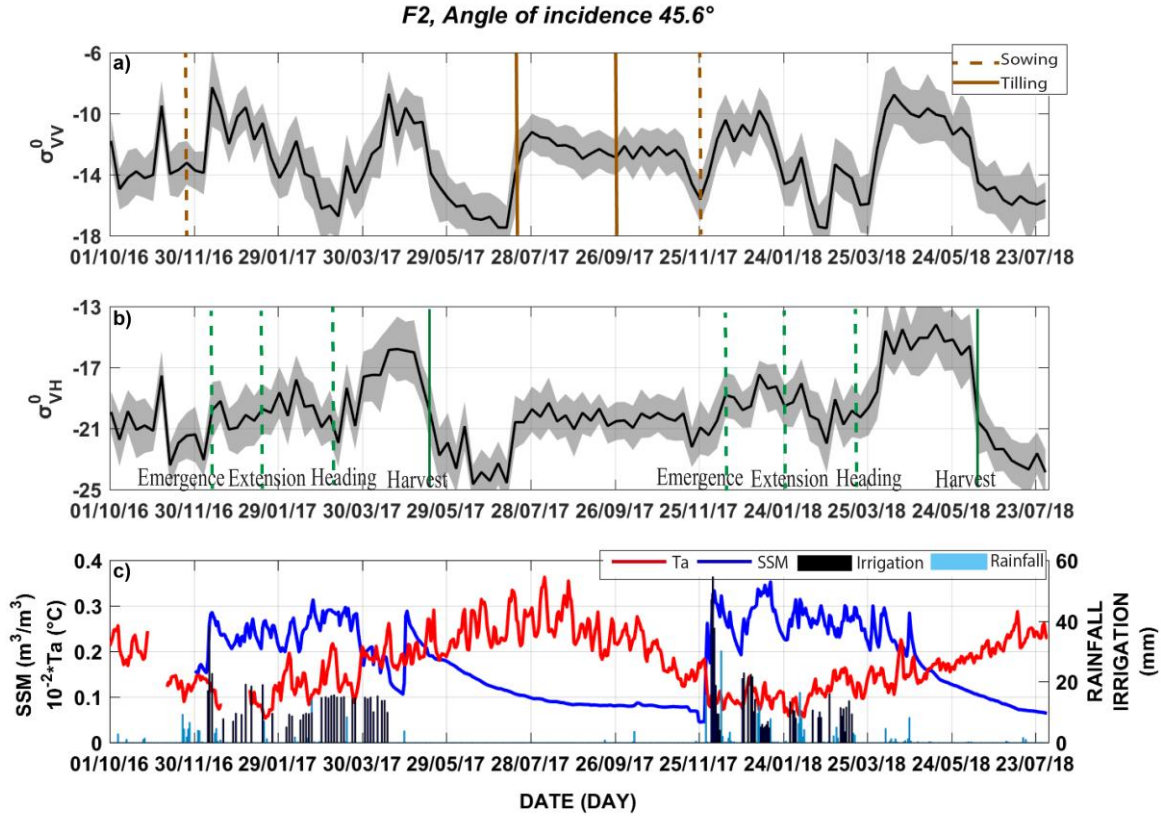
366 **4.2.1 The backscattering coefficient**

367 Figure 9 displays the time series at 45.6° over F2 for illustration purposes: a) backscattering coefficient at VV polarization  
 368 ( $\sigma_{VV}^0$ ); b) backscattering coefficient at VH polarization ( $\sigma_{VH}^0$ ) as well as wheat phenological stages; c) SSM, air temperature,

369 irrigation and rainfall. Figures A3- A5 in appendix A show the same time series over F1 and F2 at 35.2° and F1 at 45.6°,  
370 respectively. The backscattering coefficients reveal a strong seasonal signal with two cycles. The first cycle takes place from  
371 sowing to the heading stage and the second from heading to harvest with the minimum reached around the heading stage.  
372 The highest values at 35.2° are observed in the first cycle, while at 45.6°,  $\sigma^\circ$  is higher on the second peak. The maximum  
373 values of  $\sigma_{VV}^0$  reached the same value for F1 and F2 while higher values are observed on F2 at VH.  $\sigma_{VV}^0$  is more sensitive to  
374 soil moisture variation until mid-January, corresponding to the tillering stage, when the soil is not yet fully covered by  
375 vegetation. Although it is agreed that the signal during this period is governed by the dynamics of soil moisture, its behavior  
376 differs from one site to another giving the difference in soil hydric conditions and surface roughness. After this period, the  
377 signal behavior is similar to the profiles obtained by Cookmartin et al. (2000), El Hajj et al. (2019), Nasrallah et al. (2019)  
378 and Veloso et al. (2017). It decreases gradually from the early tillering until the heading stage (around March 13) by about  
379 10 dB on F2 and 5 dB on F1 because of the attenuation by the canopy during the development of the stems (extension stage)  
380 (Cookmartin et al., 2000; Mattia et al., 2003; Picard et al., 2003; Wang et al., 2018). Obviously, the attenuation is more  
381 important at VV polarization because of the vertical structure of wheat (stems) in line with the results of (Fontanelli et al.,  
382 2013; Picard et al., 2003; Wang et al., 2018). The response of  $\sigma_{VH}^0$  to SSM variation and canopy attenuation is lower than for  
383  $\sigma_{VV}^0$ . After the heading stage, the signal starts to increase again. This is clearer on F2 than F1 and at 45.6° than at 35.2°. The  
384 heading stage is the phenological stage of wheat when the spike or head starts emerging out from the leaf sheath. This  
385 change of the structure of the canopy shield the stems for the radar signal through the appearance of a thick, wet top layer  
386 composed of the heads. The C-band wavelength penetrates this layer only, resulting in increased volume scattering, while  
387 attenuation becomes low. This effect is stronger for F2 than for F1, at VH than at VV and at 45.6° than at 35.2°. This  
388 increase was first reported by Ulaby and Batlivala (1976). Subsequently, Ulaby et al. (1986) suggested that an additional  
389 term must be added to the traditional three-term model (vegetation volume diffusion, soil attenuation, and soil-vegetation  
390 interaction) to properly represent wheat backscattering after heading. Later on, similar behaviour has been observed and  
391 attributed to the appearance of the heads followed by the grain by numerous authors (Brown et al., 2003; El Hajj et al., 2019;  
392 Mattia et al., 2003; Patel et al., 2006; Veloso et al., 2017). The exceptional growing conditions on F2 during S2 is at the  
393 origin of the observed plateau of the backscattering coefficient which remains quite stable until harvest. This is due to a  
394 significant contribution of volume scattering which is a behavior that characterize a crop developing a random canopy  
395 structure in relation to the numerous and dense adventices as already highlighted (cf. picture Fig. A1 at appendix A).

396 The low variation observed on F1 during the 2016-2017 season is mainly related to the limited development of vegetation  
397 because of the triggered water stress. Likewise, the difference between the two seasons over F2 is related to a higher density  
398 of grown seeds and wetter conditions in the 2017-2018 season compared to 2016-2017 (the amount of rainfall during the  
399 growing season-from sowing to harvest-reached 167.23 mm in 2017-2018 while only 69.94 mm is recorded in 2016-2017).  
400 With the drying of the head layer, the backscattering decreases again at the end of the season to reach the lower observed  
401 values. Indeed, as the head layer dries, the vegetation becomes transparent to the signal. The soil is also dry at the end of the

402 season because irrigation is stopped. These low values remained until the first deep ploughing on July 11, when a sharp  
 403 increase is observed because of a drastic change of soil roughness. Hereafter, the signal is again stable until the seedling  
 404 preparation work for the next 2017-2018 season (November 22).



405  
 406 **Figure 9.** Time series of the backscattering coefficient at VV (a) and VH (b) polarizations on F2 at 45.6° of incidence angle during  
 407 the period from October 01, 2016 to July 31, 2018. The tilling works and phenological stages of wheat are superimposed on  
 408 subplots (a) and (b), respectively. The air temperature, surface soil moisture (SSM), irrigation and rainfall are displayed on  
 409 subplot (c).

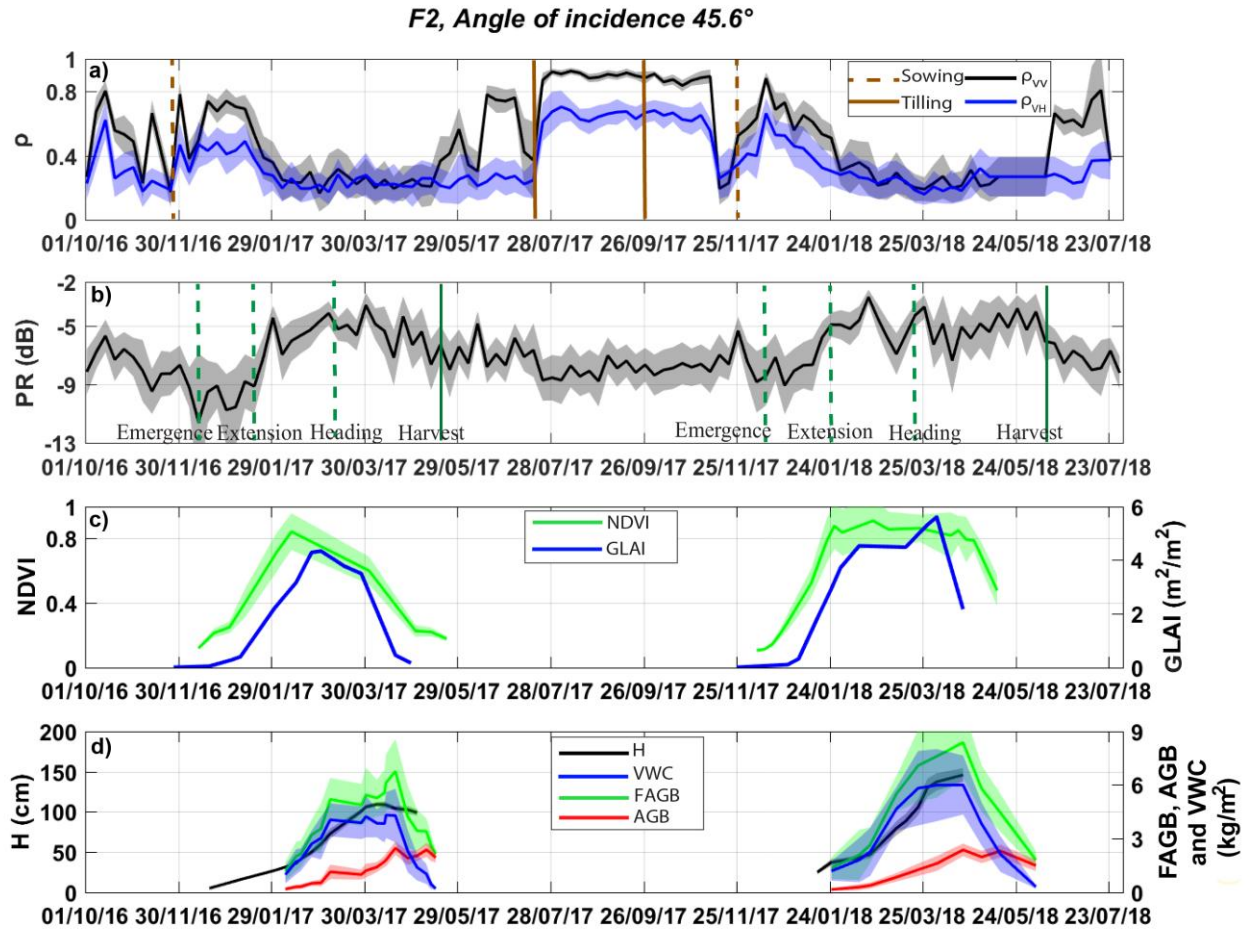
#### 410 4.2.2 The interferometric coherence and the polarization ratio

411 Figure 10 displays the time series at 45.6° over F2 of: a) interferometric coherence at VV ( $\rho_{VV}$ ) and VH ( $\rho_{VH}$ ) polarizations  
 412 together with sowing and tilling dates; b) polarization ratio ( $PR = \sigma_{VH}^0 / \sigma_{VV}^0$ ), as well as wheat phenological stages; c)  
 413 Sentinel-2 NDVI and measured GLAI; d) Measured FAGB, AGB, VWC and H. Likewise, Fig. A6- Fig. A8 in appendix A  
 414 display the time series over F1 and F2 at 35.2° and F1 at 45.6°, respectively. The time series of  $\rho_{VV}$  and  $\rho_{VH}$  follows a  
 415 similar evolution. Before sowing, coherence is at its highest value corresponding to 0.9 for  $\rho_{VV}$  and 0.7 for  $\rho_{VH}$  (Fig. 10a).  
 416 These values express a dominance of coherent scattering, corresponding to response of bare soils composed of big rocks.  
 417 Indeed, during the summer, the plots are subjected to deep ploughing which yields big clods that resist any change in surface

418 structure caused by climatic factors such as wind or rain. The second tilling breaks up the clods for the next seeding. Soil  
419 works and farming activities induce a large decrease in coherence in line with the observation of Wegmuller and Werner  
420 (1997). The surface roughness is a main parameter that influences not only the amplitude at C-band but also the phase.  
421 Indeed, abrupt drops are observed around each sowing events and tilling works (brown vertical lines on Fig. 10a).

422 After sowing, the evolution is similar to the profiles obtained by Blaes and Defourny (2003) and Engdahl et al. (2001). The  
423 interferometric coherence increases from 0.15 to 0.7 and then starts to decrease slightly from the emergence of wheat,  
424 becoming almost constant after stem extension with values  $< 0.3$  corresponding to the noise level. Indeed, using the ERS-  
425 Envisat Tandem mission, Santoro et al., (2010) demonstrated that coherence measurements of vegetated fields are always  
426 below the level of bare soils coherence. Actually, the interferometric coherence is known to decrease exponentially with  
427 wheat growth (Lee et al., 2012). Vegetation growth and random dislocation of scatters cause a degradation of coherence  
428 (Blaes and Defourny, 2003; Engdahl et al., 2001; Wegmuller and Werner, 1997), especially under wind and rain effects.  
429 Between sowing and emergence, the observed variation is assumed to be related to the installation of irrigation drippers that  
430 took place up to two weeks after sowing. The changes that occur between the harvest and the first tilling could be attributed  
431 to livestock grazing, a common practice in the region after wheat harvest, which could change the surface roughness.

432 The polarization ratio (PR) is closely related to the biomass dynamic. Both are increasing from emergence to heading and  
433 then start to decrease until harvest. The maximum timing is around middle of April. The significant differences in  
434 biophysical parameters between F1 and F2 is due to irrigation, as already highlighted for the backscattering coefficient time  
435 series. Likewise, the difference between the two seasons over F2 is related to a higher sowing density and wetter conditions  
436 in the 2017-2018 season compared to 2016-2017. As shown above (Fig. 8), the time series of FAGB and VWC are in line  
437 with AGB and H up to the peak of FAGB and then decrease together while AGB continues to increase and H remains at its  
438 maximum value. FAGB and VWC are dropping at the same time but 50 days after when compared to GLAI and NDVI and  
439 about 15 days before the backscattering coefficient.



440  
 441 **Figure 10.** Time series of the interferometric coherence at VV and VH polarizations (a) and the polarization ratio (b) on F2 at  
 442 **45.6°** of incidence angle during the period from October 01, 2016 to July 31, 2018. The tilling works and phenological stages of  
 443 wheat are superimposed on subplots (a) and (b), respectively. NDVI and measured GLAI are displayed in subplot (c). Measured  
 444 H, FAGB, VWC and AGB are plotted in subplot (d). Time series are presented by mean values (solid lines) and standard  
 445 deviations (filled fields surrounding the solid lines).

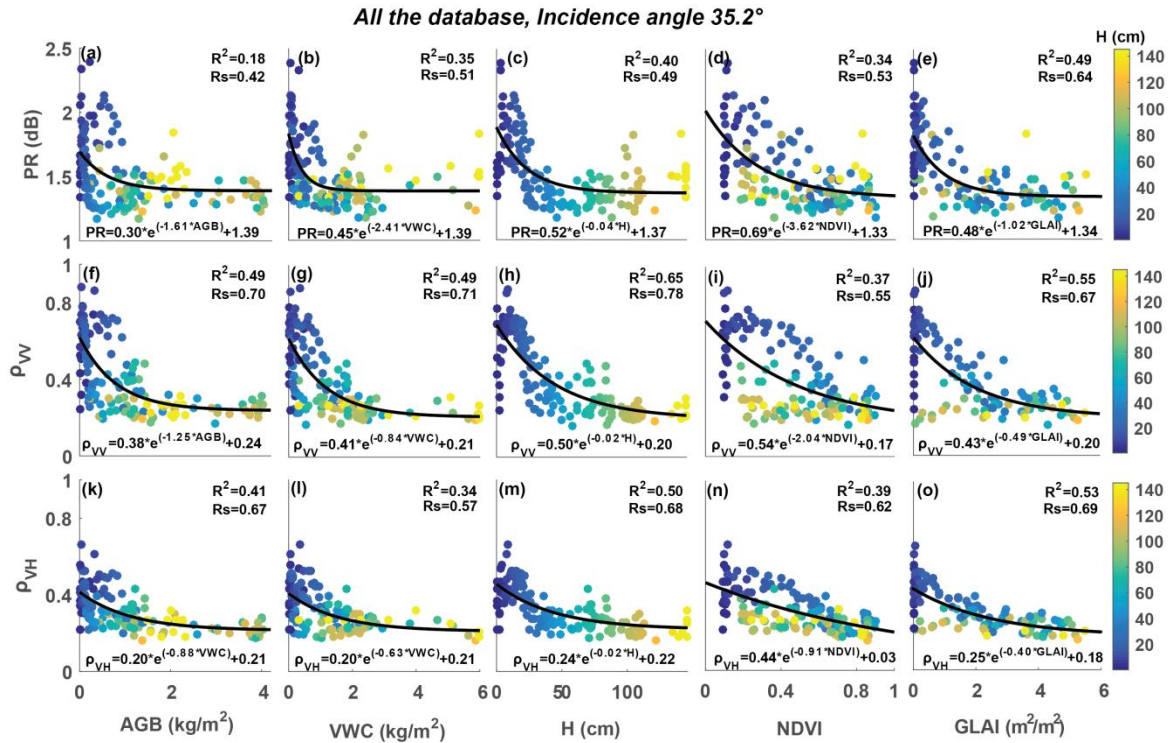
#### 446 4.3 Relationship between SAR data and vegetation variables

447 The polarization ratio and the interferometric coherence have been shown to be related to vegetation growth. In this section,  
 448 the relationships between PR,  $\rho_{VV}$  and  $\rho_{VH}$  and vegetation variables, including AGB, VWC, H, GLAI and NDVI are  
 449 analyzed. Figure 11 displays the results at 35.2° of incidence angle and Fig. A9 in appendix A displays the results at 45.6°. H  
 450 is used to illustrate the vegetation growth because its evolution is monotonic, so that data corresponding to before and after  
 451 maximum development can be easily separated. The determination coefficient  $R^2$  and the Spearman rank correlation  $R_s$  are  
 452 superimposed on the subplots together with the fitting equations using the whole database. Overall, a good correlation has

453 been found between SAR variables (PR,  $\rho_{VV}$  and  $\rho_{VH}$ ) and AGB, VWC, GLAI and H. A hysteresis behavior is obviously  
454 observed for the vegetation variables with a non-monotonic dynamic (VWC, NDVI and GLAI). Using PR, the relationships  
455 are more scattered and characterized by lower saturation value. Although the range of variation of  $\rho_{VH}$  is limited with  
456 regards to PR, the statistical metrics of the relationships between interferometric coherences and the vegetation variables are  
457 better than those obtained using PR.  $\rho_{VV}$  exhibited better correlation to the vegetation variables than  $\rho_{VH}$ . With the exception  
458 of NDVI, Rs is always greater than 0.67. The best fit is obtained between  $\rho_{VV}$  and H (Rs = 0.78 and  $R^2 = 0.65$ ) with higher  
459 saturation value than the other relationships (~55% of H range which is about 77 cm). By contrast, a visual inspection of the  
460 Fig. 11 (d, i and n) shows that relationships with NDVI are poorer when using data of the whole growing season. The  
461 dispersion is strong along the season. Data before and after the maximum development can be distinguished, particularly,  
462 using  $\rho_{VV}$  and to a lesser extent  $\rho_{VH}$ . Figure 11 (i and n) shows that a linear relationship exists between NDVI and SAR data  
463 using data before maximum development only, i.e. when the vegetation is still green. During the beginning of the season, the  
464 slope of  $\rho_{VV}$ -NDVI and  $\rho_{VH}$ -NDVI is low compared to the other vegetation variables. This is because the NDVI increases  
465 faster around the emergence of wheat while  $\rho_{VV}$  is steel high because of the low vegetation cover fraction at this time. The  
466 hysteresis effect observed after the maximum of vegetation development is due to the senescence of the leaves when NDVI  
467 starts decreasing while  $\rho_{VV}$  and  $\rho_{VH}$  are stable at low values.

468 When considering SAR data at 45.6° of incidence angle (Fig. A9), a similar behavior to Fig. 11 is observed with AGB,  
469 VWC, H and NDVI. Same hysteresis and scattering are observed for NDVI although higher correlations are obtained.  
470 Similarly,  $\rho_{VV}$  is better correlated to vegetation parameter than  $\rho_{VH}$  and PR. By contrast, GLAI is better correlated with SAR  
471 variables than H. The PR-GLAI relationship is more scattered than at 35.2° while  $\rho_{VV}$ -GLAI has the best metrics (Rs = 0.82  
472 and  $R^2 = 0.73$ ) with a higher saturation value around 50% of the GLAI range (3 m<sup>2</sup> m<sup>-2</sup>).

473 Unlike PR, the metrics at both 35.2° and 45.6° are stable for the relationships between  $\rho_{VV}$  with AGB, VWC and H. By  
474 contrast, PR-GLAI is more stable than  $\rho_{VV}$ -GLAI at both incidence angles.



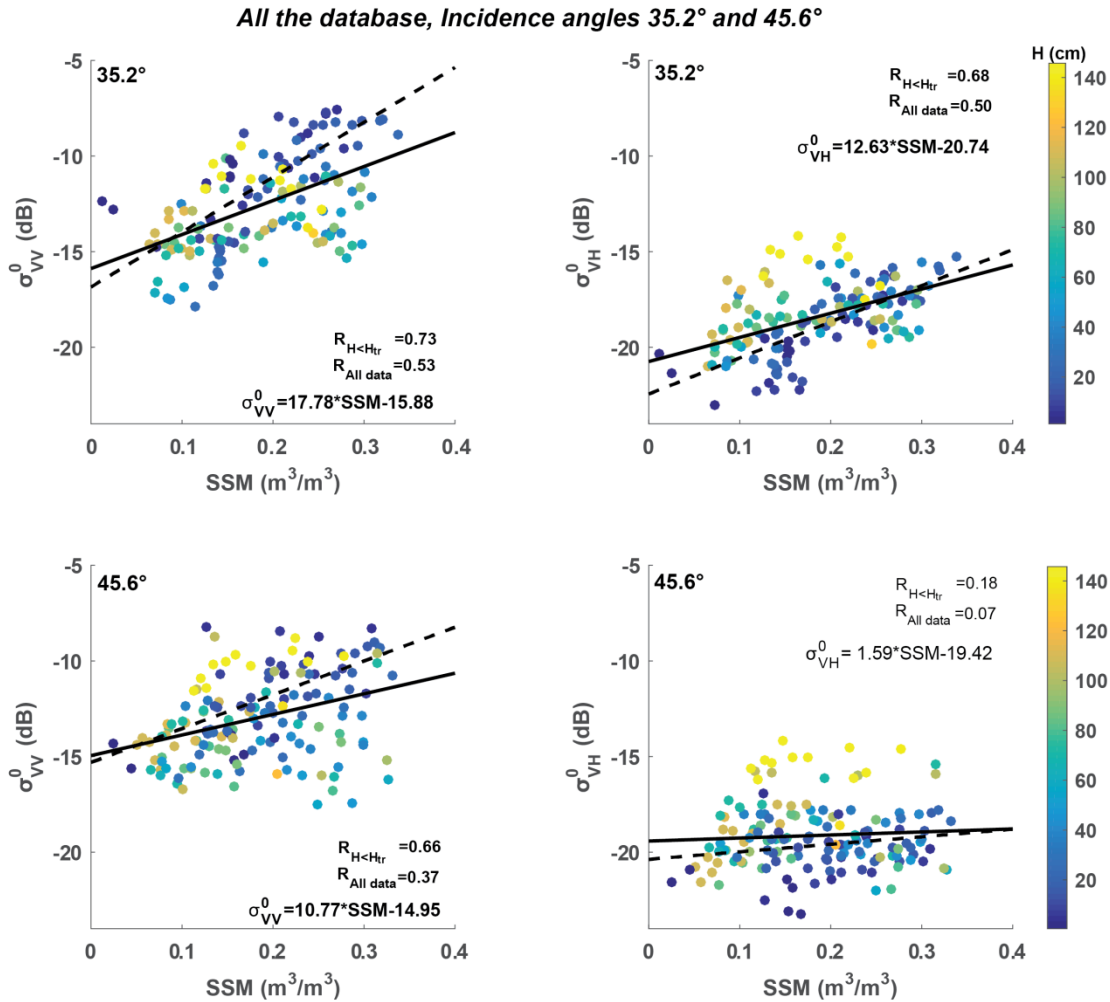
475

476 **Figure 11. Scatter plots of the relationships between PR,  $\rho_{VV}$  and  $\rho_{VH}$  and AGB, VWC, H, NDVI and GLAI at 35.2° angle of**  
 477 **incidence. The entire database is used from the three fields (F1, F2 and F3). H is used to monitor the evolution during the growing**  
 478 **season. All the determination coefficient  $R^2$  and the Spearman rank correlation  $R_s$  are significant at 99%.**

#### 479 4.4 Relationship between backscattering coefficient and SSM

480 Figure 12 displays the relationships between  $\sigma^0$  and SSM using the entire database at 45.6° and 35.2° of incidence angles. H  
 481 is used as an indicator of vegetation growth. The correlation coefficient is computed separately for the entire database and  
 482 for data corresponding to H lower than a threshold value ( $H_{tr}$ ) correspond to  $GLAI < 1.5$ . This value of GLAI correspond to  
 483 wheat not fully covering the soil (Ouadi et al., 2020b).  $H_{tr}$  is about 23.5 cm, 23.5 cm, 32.9 cm and 26 cm for F1 and F2  
 484 during 2017-2018, for F2 during 2016-2017 and for F3. Overall,  $\sigma_{VV}^0$  is obviously better correlated to SSM than  $\sigma_{VH}^0$  in line  
 485 with the results of numerous studies (Holah et al., 2005; Li et al., 2014; Ulaby and Batlivala, 1976). Likewise, metrics at  
 486 35.2° are better than those obtained at 45.6°. This is expected as the contribution of vegetation is dominant at higher  
 487 incidence angles and at VH polarization. The relationships are scattered when using data from the whole season. This is  
 488 attributed to the presence of vegetation and mainly to the attenuation of the soil signal backscattered by the wheat. The  
 489 sensitivity of  $\sigma^0$  to SSM decreases progressively during the growing season as shown by the decreasing slope of the  
 490 relationships with the vegetation development. By considering the early season data only, when the soil is not yet covered by

491 vegetation, a better fitting is obtained between  $\sigma^0$  and SSM. Indeed, the correlation coefficient using data with  $H < H_{tr}$  is  
 492 improved whatever the polarization and the incidence angle. Obviously, the highest correlation is obtained at VV  
 493 polarization and  $35.2^\circ$  of incidence angle ( $R = 0.73$ ) and to a lesser extent at VV at  $45.6^\circ$  and VH at  $35.2^\circ$  with  $R \geq 0.66$ .



494  
 495 **Figure 12.** Scatter plots of the relationships between  $\sigma_{VV}^0$  and  $\sigma_{VH}^0$  and SSM at  $45.6^\circ$  and  $35.2^\circ$  angles of incidence. The entire  
 496 database is used from the three fields (F1, F2 and F3). H is used to monitor the evolution during the growing season. The  
 497 significant correlation coefficients are in bold. The solid and the dashed lines correspond to all database and data with  $GLAI < 1.5$ ,  
 498 respectively.

## 499 **5 Conclusion**

500 This paper presents a 3-year database of C-band radar data and all necessary ancillary ground measurements to improve our  
501 understanding of the radar signal and to develop inversion methods for land surface parameters retrieval. The data are  
502 collected from three heavily monitored wheat fields under semi-arid conditions in the center of Morocco. The database offers  
503 a complete set of data for radar applications on wheat monitoring. The measured parameters include fresh and dry above  
504 ground biomass, canopy height, leaf area index, cover fraction, surface soil moisture, root zone soil moisture and surface  
505 roughness, in addition to the normalized difference vegetation index and SAR data (the backscattering coefficient and the  
506 interferometric coherence). The irrigation and meteorological data are also provided. This database opens the opportunity to  
507 use remote sensing together with measured parameters to understand and investigate the behavior of wheat crops and  
508 thereafter for vegetation parameters and soil moisture retrieval. The database analysis presented in this paper demonstrates  
509 the potentialities of SAR data for wheat monitoring by addressing the well-known sensitivity of SAR to surface soil moisture  
510 and vegetation variables. The obtained relationships between SAR measurements including backscattering coefficient,  
511 polarization ratio and interferometric coherence can be used for the application of several backscattering models, the  
512 retrieval of biophysical variables and for yield prediction in crop models. They can also be useful for land surface models  
513 relying on accurate estimation of vegetation height such as the energy balance models (i.e. TSEB -Two Source Energy  
514 Balance- Norman et al., 1995). The dataset illustrates also the complex signal acquired by C-band radar over wheat crops  
515 that is not yet fully understood as it mix the responses from highly dynamic contributions of soil and vegetation elements.  
516 The unique dataset provided in this paper should contribute through future studies to improve our understanding of the  
517 response of C-band radar observations over annual crops.

## 518 **6 Database availability**

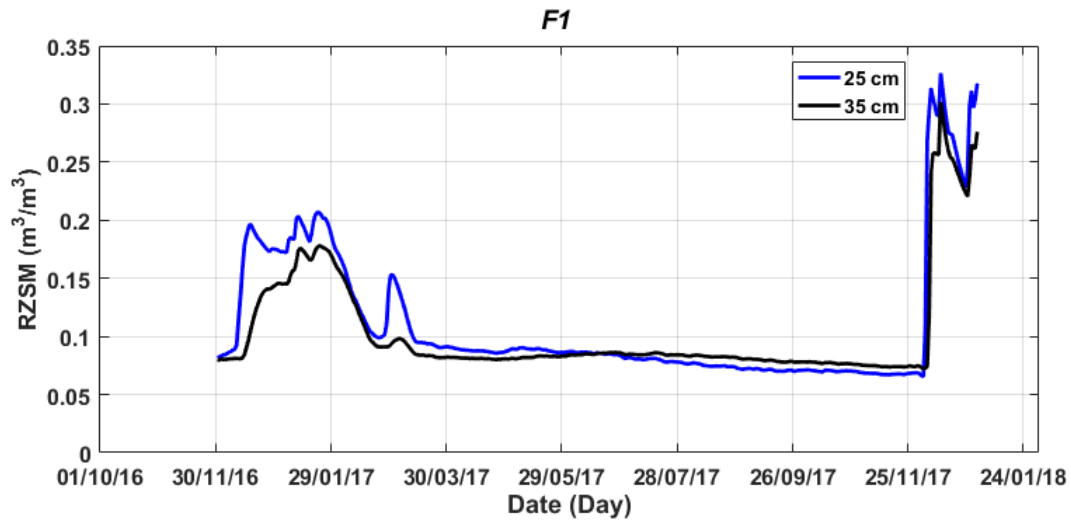
519 This database is archived in DtaSuds repository of the French National Research Institute for Sustainable Development  
520 (IRD). The database is accessible free of charge with "CC-BY" licence at <https://doi.org/10.23708/8D6WQC> (Ouaadi et al.,  
521 2020a). It can be downloaded as xlsx files accompanied by a variable dictionary containing the variable names and units.  
522 The files are also accompanied by a metadata including a description of the database, time coverage, keywords and other  
523 general information.

524



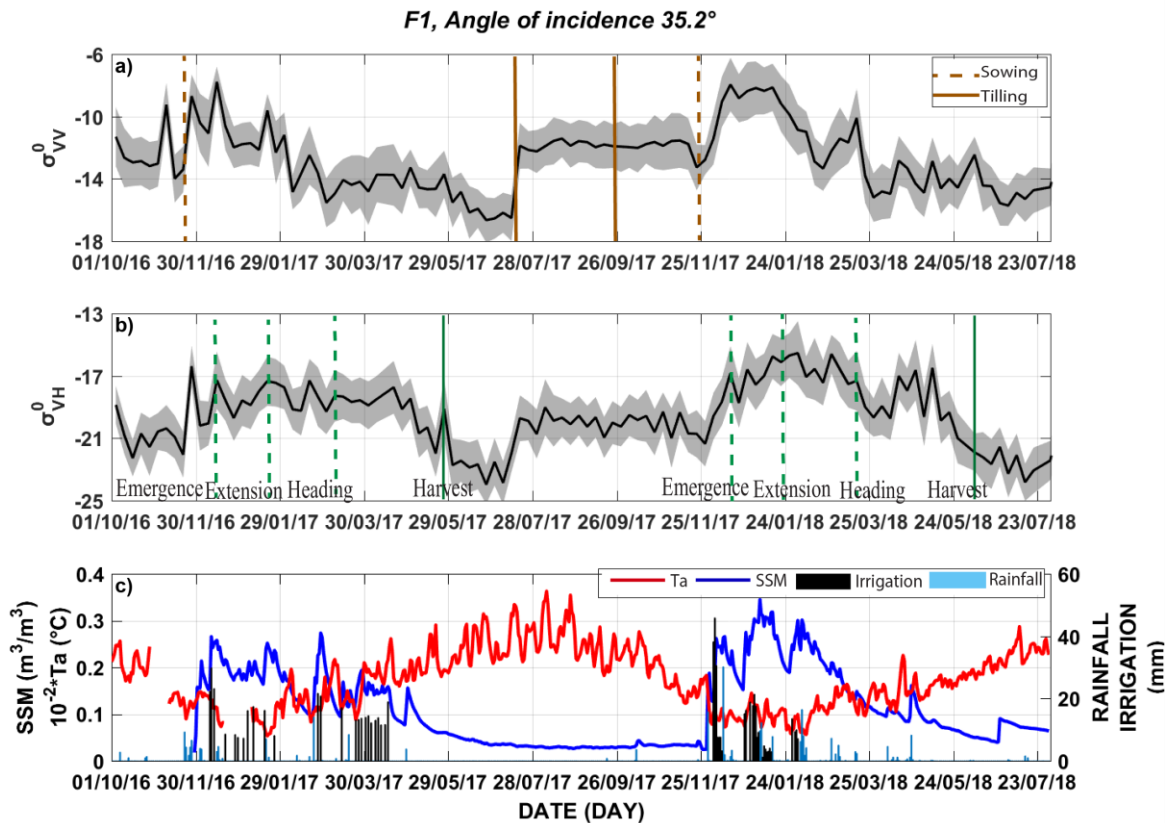
526

527 **Figure A1. Picture taken over F2 during 2017-2018 growing season (14/05/2018) illustrates the specific growing conditions**  
528 **(adventices and stems laid down by wind).**

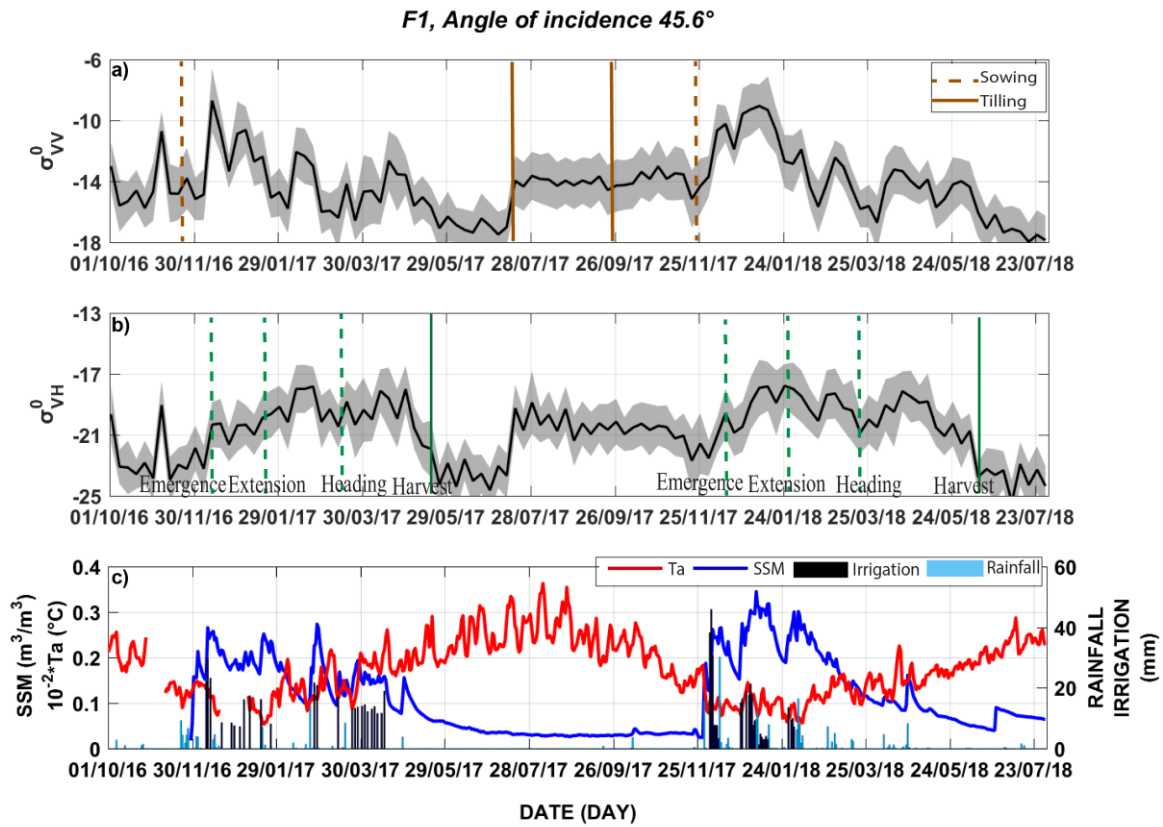


530

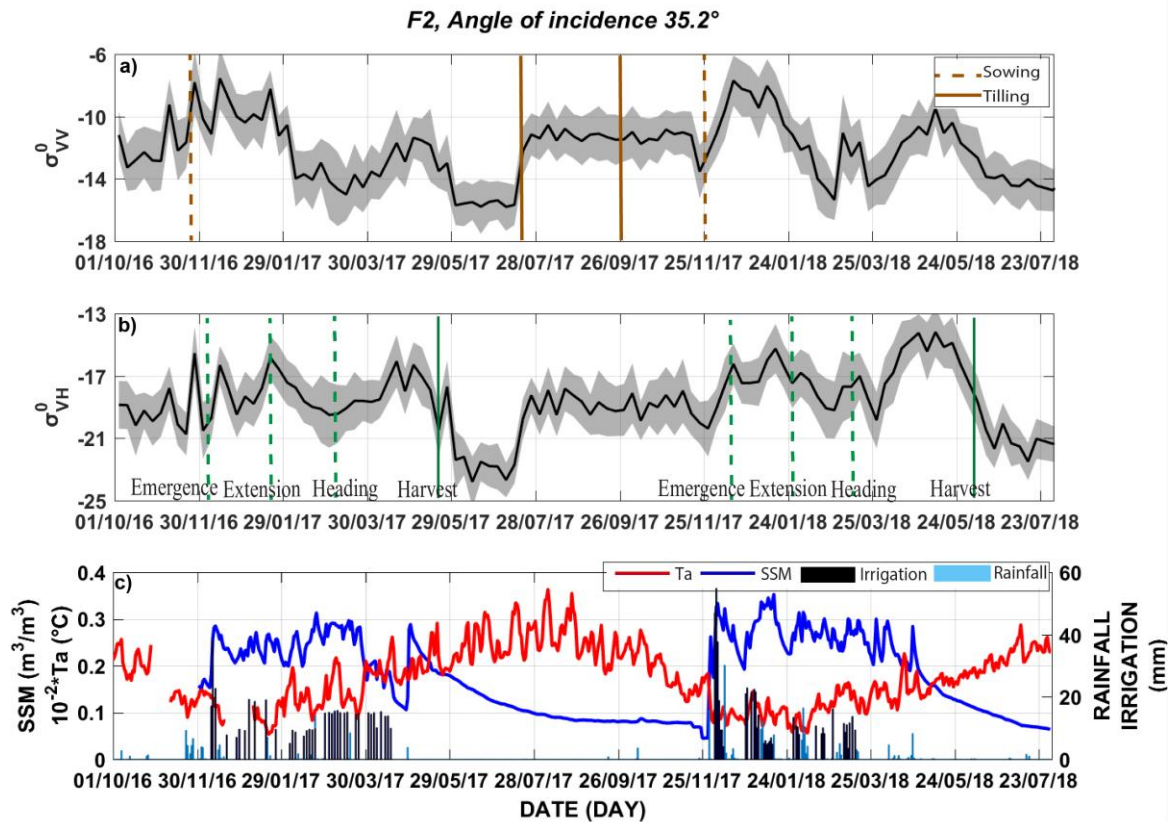
531 **Figure A2.** Time series of root zone soil moisture (RZSM) at 25 and 35 cm of depth measured over F1 from December 01, 2016 to  
532 **December 31, 2017.**



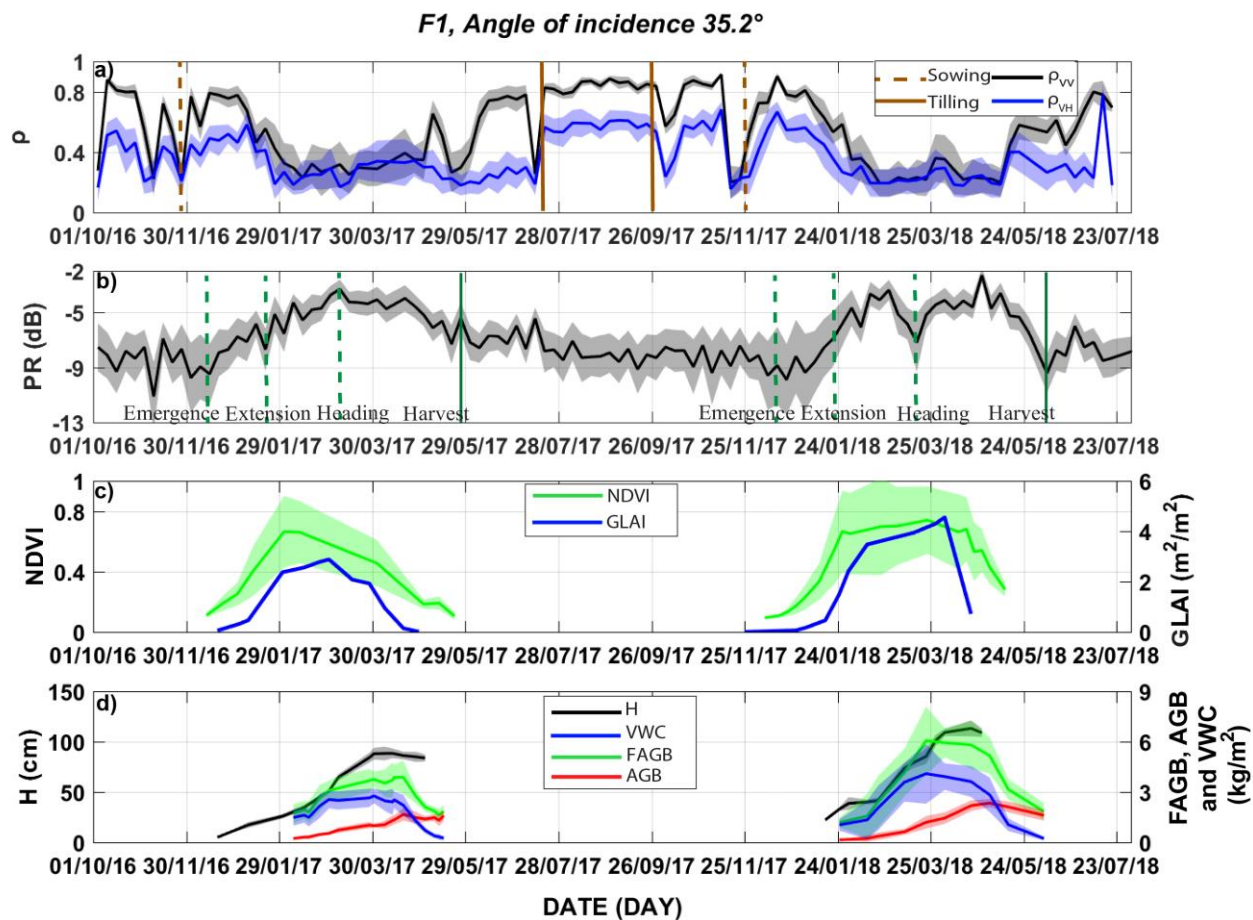
533  
 534 **Figure A3.** Time series of the backscattering coefficient at VV (a) and VH (b) polarizations on F1 at 35.2° of incidence angle during  
 535 the period from October 01, 2016 to July 31, 2018. The tilling works and phenological stages of wheat are superimposed on  
 536 subplots (a) and (b), respectively. The air temperature, Surface soil moisture (SSM), irrigation and rainfall are displayed on  
 537 subplot (c).



538  
 539 **Figure A4.** Time series of the backscattering coefficient at VV (a) and VH (b) polarizations on F1 at 45.6° of incidence angle during  
 540 the period from October 01, 2016 to July 31, 2018. The tilling works and phenological stages of wheat are superimposed on  
 541 subplots (a) and (b), respectively. The air temperature, Surface soil moisture (SSM), irrigation and rainfall are displayed on  
 542 subplot (c).

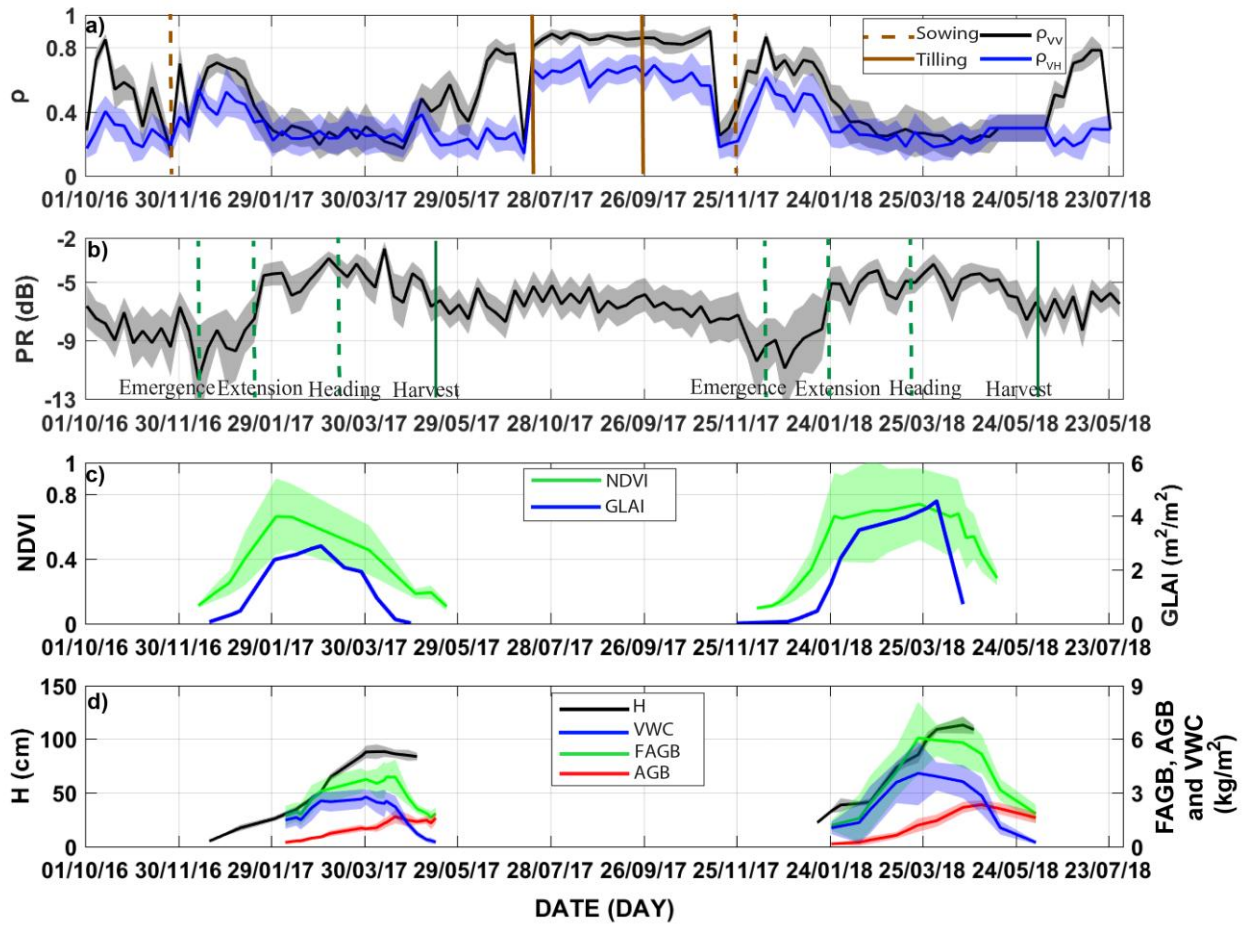


543  
 544 **Figure A5.** Time series of the backscattering coefficient at VV (a) and VH (b) polarizations on F2 at 35.2° of incidence angle during  
 545 the period from October 01, 2016 to July 31, 2018. The tilling works and phenological stages of wheat are superimposed on  
 546 subplots (a) and (b), respectively. The air temperature, Surface soil moisture (SSM), irrigation and rainfall are displayed on  
 547 subplot (c).

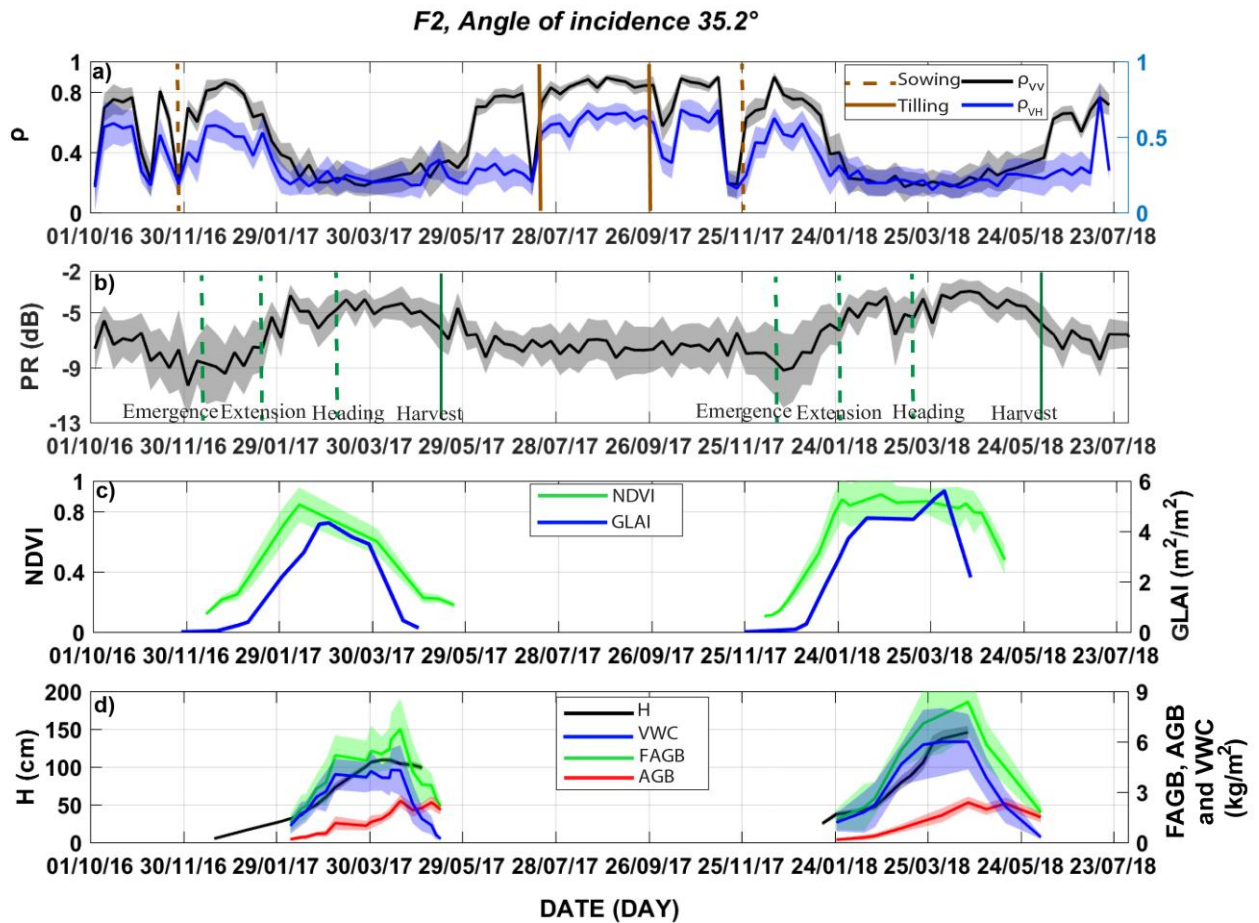


548  
 549 **Figure A6.** Time series of the interferometric coherence at VV and VH polarizations (a) and the polarization ratio (b) on F1 at  
 550 35.2° of incidence angle during the period from October 01, 2016 to July 31, 2018. The tilling works and phenological stages of  
 551 wheat are superimposed on subplots (a) and (b), respectively. NDVI and measured GLAI are displayed in subplot (c). Measured  
 552 H, FAGB, VWC and AGB are plotted in subplot (d). Time series are presented by mean values (solid lines) and standard  
 553 deviations (filled fields surrounding the solid lines).

F1, Angle of incidence 45.6°

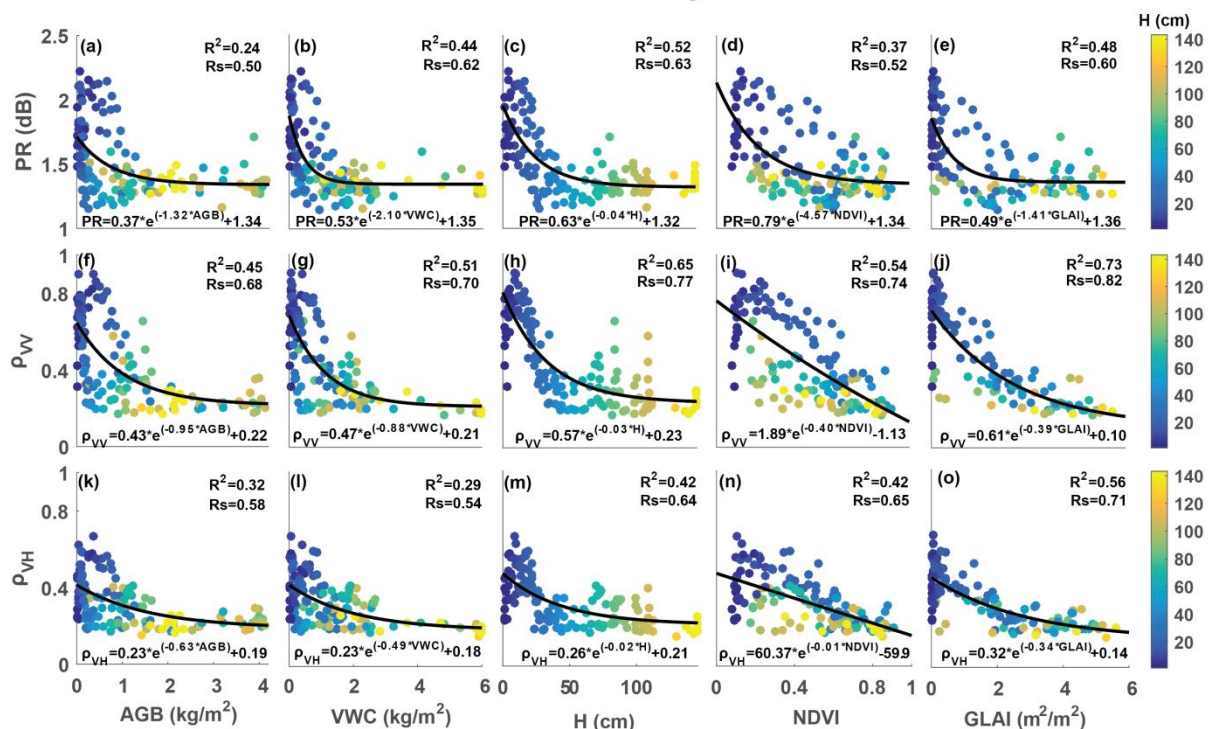


554  
 555 **Figure A7.** Time series of the interferometric coherence at VV and VH polarizations (a) and the polarization ratio (b) on F1 at  
 556 45.6° of incidence angle during the period from October 01, 2016 to July 31, 2018. The tilling works and phenological stages of  
 557 wheat are superimposed on subplots (a) and (b), respectively. NDVI and measured GLAI are displayed in subplot (c). Measured  
 558 H, FAGB, VWC and AGB are plotted in subplot (d). Time series are presented by mean values (solid lines) and standard  
 559 deviations (filled fields surrounding the solid lines).



560  
 561 **Figure A8.** Time series of the interferometric coherence at VV and VH polarizations (a) and the polarization ratio (b) on F2 at  
 562 35.2° of incidence angle during the period from October 01, 2016 to July 31, 2018. The tilling works and phenological stages of  
 563 wheat are superimposed on subplots (a) and (b), respectively. NDVI and measured GLAI are displayed in subplot (c). Measured  
 564 H, FAGB, VWC and AGB are plotted in subplot (d). Time series are presented by mean values (solid lines) and standard  
 565 deviations (filled fields surrounding the solid lines).

All the database, Incidence angle 45.6°



566

567 Figure A9. Scatterplots of the relationships between PR,  $\rho_{VV}$  and  $\rho_{VH}$  and AGB, VWC, H, NDVI and GLAI at 45.6° angle of  
 568 incidence. The entire database is used from the three fields (F1, F2 and F3). H is used to monitor the evolution during the growing  
 569 season. All the determination coefficient  $R^2$  and the Spearman rank correlation  $R_s$  are significant at 99%.

570

571 Table A1. Details of the field campaigns during the 2016-2017, 2017-2018 and 2018-2019 agricultural seasons.

2016-2017 saison								2017-2018 saison								2018-2019 saison							
Date	$h_{rms}$ & L	H	Fc	LAI	AGB	FAGB	VWC	Date	$h_{rms}$ & L	H	Fc	LAI	AGB	FAGB	VWC	Date	$h_{rms}$ & L	H	Fc	LAI	AGB	FAGB	VWC
29/11/2016	x							21/12/2017	x							29/11/2018	x		x	x			
30/11/2016	x							28/12/2017	x		x	x				07/12/2018			x	x			
09/12/2016	x							04/01/2018	x		x	x				12/12/2018	x						
20/12/2016	x	x	x	x				16/01/2018	x	x	x	x				18/12/2018			x	x			
03/01/2017	x		x	x				25/01/2018	x	x	x	x	x	x	x	04/01/2019	x		x	x			
09/01/2017	x	x	x	x				31/01/2018	x	x	x	x				15/01/2019	x	x	x	x	x	x	x
31/01/2017	x	x	x	x				12/02/2018		x	x	x	x	x	x	01/02/2019		x	x	x	x	x	x
07/02/2017					x	x	x	19/02/2018		x						13/02/2019		x	x	x	x	x	x
14/02/2017	x	x	x	x	x	x	x	08/03/2018		x			x	x	x	04/03/2019		x	x	x	x	x	x
17/02/2017		x			x	x	x	14/03/2018		x	x	x	x	x	x	13/03/2019		x	x	x	x	x	x
24/02/2017		x	x	x	x	x	x	22/03/2018		x			x	x	x	26/03/2019		x	x	x			
02/03/2017		x	x	x	x	x	x	28/03/2018		x	x	x				03/04/2019		x					
08/03/2017		x			x	x	x	03/04/2018		x	x	x	x	x	x	09/04/2019		x			x	x	x
17/03/2017			x	x				20/04/2018		x	x	x	x	x	x	16/04/2019		x					
28/03/2017		x	x	x	x	x	x	27/04/2018		x						20/04/2019		x			x	x	x
31/03/2017		x			x	x	x	02/05/2018					x	x	x	27/04/2019		x			x	x	x
07/04/2017		x	x	x	x	x	x	14/05/2018					x	x	x								
12/04/2017		x			x	x	x	06/06/2018					x	x	x								
13/04/2017					x	x	x																
19/04/2017		x	x	x	x	x	x																
27/04/2017		x			x	x	x																
29/04/2017			x	x																			
03/05/2017		x			x	x	x																
09/05/2017					x	x	x																
12/05/2017					x	x	x																
15/05/2017					x	x	x																

572

573 **Author contribution.** NO, LJ, JE and SK designed the experiments. NO, MK, JE, AC and AB carried the experiments out.  
574 NO processed the Sentinel-1 products. NO, LJ, JE and SK analyzed the data. NO wrote the original draft and all the co-  
575 authors contribute in the review and editing of the manuscript.

576 **Competing interests.** The authors declare that they have no conflict of interest.

577 **Acknowledgement.** The database is collected within the framework of the International Joint Laboratory TREMA  
578 (<https://www.lmi-trema.ma/>). Omar Rafi, the owner of the private farm in which the three fields are located is  
579 acknowledged. We would like to thank the projects: Rise-H2020-ACCWA (grant agreement no: 823965), ERANETMED03-  
580 62 CHAAMS, PHC TBK/18/61 and MISTRALS/SICMED program. We thank also the Moroccan CNRST for awarding a  
581 PhD scholarship to Nadia Ouaadi. Finally, ESA and Theia are acknowledged for providing free products of Sentinel-1 and  
582 Sentinel-2 (corrected from atmospheric effects), respectively.

- 584 Abourida, A., Simonneaux, V., Errouane, S., Sighir, F., Berjami, B. and Sgir, F.: Estimation des volumes d'eau pompés dans la nappe pour  
585 l'irrigation (Plaine du Haouz, Marrakech, Maroc). Comparaison d'une méthode statistique et d'une méthode basée sur l'utilisation de  
586 données de télédétection, *J. Water Sci.*, 21(4), 489–501 [online] Available from: <https://hal.ird.fr/ird-00389822>, 2008.
- 587 Allen, R. G., Pereira, L. S., RAES, D. and SMITH, M.: Crop Evapotranspiration—Guidelines for Computing Crop Water Requirements,  
588 Irrigation and Drain, Paper No. 56. FAO, Rome, Italy,. [online] Available from: [http://academic.uprm.edu/abe/backup2/tomas/fao\\_56.pdf](http://academic.uprm.edu/abe/backup2/tomas/fao_56.pdf),  
589 1998.
- 590 Allmaras, R. R., Burwell, R. E., Larson, W. E. and Holt, R. F.: Total Porosity And Random Roughness Of The Interrow Zone As  
591 Influenced By Tillage, Usa. [online] Available from: <https://www.ars.usda.gov/ARSTUserFiles/50701000/cswq-t1914-allmaras.pdf>  
592 (Accessed 21 February 2020), 1966.
- 593 Bai, X., He, B., Li, X., Zeng, J., Wang, X., Wang, Z., Zeng, Y. and Su, Z.: First assessment of Sentinel-1A data for surface soil moisture  
594 estimations using a coupled water cloud model and advanced integral equation model over the Tibetan Plateau, *Remote Sens.*, 9(7), 1–20,  
595 doi:10.3390/rs9070714, 2017.
- 596 Bamler, R. and Hartl, P.: Synthetic aperture radar interferometry, *Inverse Probl.*, 14(4), 1–54, doi:10.1088/0266-5611/14/4/001, 1998.
- 597 Bigeard, G., Coudert, B., Chirouze, J., Er-Raki, S., Boulet, G. and Jarlan, L.: Estimating evapotranspiration with thermal infrared data over  
598 Agricultural landscapes: comparison of a simple energy budget model and a svat model, in *Estimation spatialisée de l'évapotranspiration à*  
599 *l'aide de données infra-rouge thermique multi-résolutions*, pp. 149–192, Toulouse., 2017.
- 600 Blaes, X. and Defourny, P.: Retrieving crop parameters based on tandem ERS 1 / 2 interferometric coherence images, *Remote Sens.*  
601 *Environ.*, 88(4), 374–385, doi:10.1016/j.rse.2003.08.008, 2003.
- 602 Brown, S. C. M., Quegan, S., Morrison, K., Bennett, J. C. and Cookmartin, G.: High-resolution measurements of scattering in wheat  
603 canopies - Implications for crop parameter retrieval, *IEEE Trans. Geosci. Remote Sens.*, 41(7 PART I), 1602–1610,  
604 doi:10.1109/TGRS.2003.814132, 2003.
- 605 Castelli, M., Anderson, M. C., Yang, Y., Wohlfahrt, G., Bertoldi, G., Niedrist, G., Hammerle, A., Zhao, P., Zebisch, M. and Notarnicola,  
606 C.: Two-source energy balance modeling of evapotranspiration in Alpine grasslands, *Remote Sens. Environ.*, 209(February), 327–342,  
607 doi:10.1016/j.rse.2018.02.062, 2018.
- 608 Chauhan, S., Shanker, H. and Patel, P.: Wheat crop biophysical parameters retrieval using hybrid-polarized RISAT-1 SAR data, *Remote*  
609 *Sens. Environ.*, 216, 28–43, doi:10.1016/j.rse.2018.06.014, 2018.
- 610 Cho, E., Choi, M. and Wagner, W.: An assessment of remotely sensed surface and root zone soil moisture through active and passive  
611 sensors in northeast Asia, *Remote Sens. Environ.*, 160, 166–179, doi:10.1016/j.rse.2015.01.013, 2015.
- 612 CNES: The ORFEO Tool Box Software Guide. [online] Available from: <https://www.orfeo-toolbox.org/packages/OTBSoftwareGuide.pdf>,  
613 2018.
- 614 Das, N. N., Mohanty, B. P., Cosh, M. H. and Jackson, T. J.: Modeling and assimilation of root zone soil moisture using remote sensing  
615 observations in Walnut Gulch Watershed during SMEX04, *Remote Sens. Environ.*, 112, 415–429, doi:10.1016/j.rse.2006.10.027, 2008.
- 616 Duchemin, B., Hadria, R., Erraki, S., Boulet, G., Maisongrande, P., Chehbouni, A., Escadafal, R., Ezzahar, J., Hoedjes, J. C. B., Kharrou,  
617 M. H., Khabba, S., Mougnot, B., Olioso, A., Rodriguez, J. C. and Simonneaux, V.: Monitoring wheat phenology and irrigation in Central  
618 Morocco : On the use of relationships between evapotranspiration , crops coefficients , leaf area index and remotely-sensed vegetation  
619 indices, *Agric. Water Manag.*, 79(1), 1–27, doi:10.1016/j.agwat.2005.02.013, 2006.
- 620 Ducrot, R., Page, C. Le, Bommel, P. and Kuper, M.: Articulating land and water dynamics with urbanization: an attempt to model natural  
621 resources management at the urban edge, *Comput. Environ. Urban Syst.*, 28, 85–106, 2004.
- 622 Dumedah, G., Walker, J. P. and Merlin, O.: Root-zone soil moisture estimation from assimilation of downscaled Soil Moisture and Ocean  
623 Salinity data, *Adv. Water Resour.*, 84, 14–22, doi:10.1016/j.advwatres.2015.07.021, 2015.
- 624 Van Emmerik, T., Steele-Dunne, S. C., Judge, J. and Van De Giesen, N.: Impact of Diurnal Variation in Vegetation Water Content on  
625 Radar Backscatter from Maize During Water Stress, *IEEE Trans. Geosci. Remote Sens.*, 53(7), 3855–3869,  
626 doi:10.1109/TGRS.2014.2386142, 2015.
- 627 Engdahl, M. E., Borgeaud, M., Member, S. and Rast, M.: The Use of ERS-1 / 2 Tandem Interferometric Coherence in the Estimation of

- 628 Agricultural Crop Heights, *IEEE Trans. Geosci. Remote Sens.*, 39(8), 1799–1806, doi:0.1109/36.942558, 2001.
- 629 Ezzahar, J., Ouaadi, N., Zribi, M., Elfarkh, J., Aouade, G., Khabba, S., Er-Raki, S., Chehbouni, A. and Jarlan, L.: Evaluation of  
630 Backscattering Models and Support Vector Machine for the Retrieval of Bare Soil Moisture from Sentinel-1 Data, *Remote Sens.*, 12(1),  
631 72, doi:10.3390/rs12010072, 2020.
- 632 Fader, M., Shi, S., Bondeau, A. and Cramer, W.: Mediterranean irrigation under climate change: more efficient irrigation needed to  
633 compensate for increases in irrigation water requirements, *Hydrol. Earth Syst. Sci.*, 20, 953–973, doi:10.5194/hess-20-953-2016, 2016.
- 634 Farineau, J. and Morot-Gaudry, J.-F.: La photosynthèse: Processus physiques, moléculaires et physiologiques, Quae., Paris. [online]  
635 Available from: <https://books.google.fr/books?id=UHBJDwAAQBAJ> (Accessed 30 August 2020), 2018.
- 636 Fieuzal, R., Baup, F. and Marais-Sicre, C.: Monitoring Wheat and Rapeseed by Using Synchronous Optical and Radar Satellite Data—  
637 From Temporal Signatures to Crop Parameters Estimation, *Adv. Remote Sens.*, 02(02), 162–180, doi:10.4236/ars.2013.22020, 2013.
- 638 Fontanelli, G., Paloscia, S., Pampaloni, P., Pettinato, S., Santi, E., Montomoli, F., Brogioni, M. and Macelloni, G.: HydroCosmo: The  
639 monitoring of hydrological parameters on agricultural areas by using Cosmo-SkyMed images, *Eur. J. Remote Sens.*, 46(1), 875–889,  
640 doi:10.5721/EuJRS20134652, 2013.
- 641 Ford, T. W., Harris, E. and Quiring, S. M.: Estimating root zone soil moisture using near-surface observations from SMOS, *Hydrol. Sci. J.*,  
642 18, 139–154, doi:10.5194/hess-18-139-2014, 2014.
- 643 Frison, P.-L. and Lardeux, C.: Vegetation Cartography from Sentinel-1 Radar Images, in *QGIS and Applications in Agriculture and Forest*,  
644 edited by N. Baghdadi, C. Mallet, and M. Zribi, p. 350., 2018. <https://doi.org/10.1002/9781119457107.ch6>
- 645 Gherboudj, I., Magagi, R., Berg, A. A. and Toth, B.: Soil moisture retrieval over agricultural fields from multi-polarized and multi-angular  
646 RADARSAT-2 SAR data, *Remote Sens. Environ.*, 115(1), 33–43, doi:10.1016/j.rse.2010.07.011, 2011.
- 647 Giorgi, F.: Climate change hot-spots, *Geophys. Res. Lett.*, 33(8), 1–4, doi:10.1029/2006GL025734, 2006.
- 648 Giorgi, F. and Lionello, P.: Climate change projections for the Mediterranean region, *Glob. Planet. Change*, 63, 90–104,  
649 doi:10.1016/j.gloplacha.2007.09.005, 2008.
- 650 Girard, M. C. (Michel C. and Girard, C. M. (Colette M.: *Télé-détection appliquée: zones tempérées et intertropicales*, Paris., edited by  
651 MASSON., 1989.
- 652 Gorrab, A., Zribi, M., Baghdadi, N., Mougnot, B., Fanise, P. and Chabaane, Z. L.: Retrieval of both soil moisture and texture using  
653 TerraSAR-X images, *Remote Sens.*, 7(8), 10098–10116, doi:10.3390/rs70810098, 2015.
- 654 Hagolle, O., Huc, M., Pascual, D. V. and Dedieu, G.: A multi-temporal method for cloud detection, applied to FORMOSAT-2, VEN $\mu$ S,  
655 LANDSAT and SENTINEL-2 images, *Remote Sens. Environ.*, 114(8), 1747–1755, doi:10.1016/j.rse.2010.03.002, 2010.
- 656 Hagolle, O., Huc, M., Pascual, D. V. and Dedieu, G.: A multi-temporal and multi-spectral method to estimate aerosol optical thickness  
657 over land, for the atmospheric correction of FormoSat-2, LandSat, VEN $\mu$ S and Sentinel-2 images, *Remote Sens.*, 7(3), 2668–2691,  
658 doi:10.3390/rs70302668, 2015.
- 659 El Hajj, M., Baghdadi, N., Zribi, M., Belaud, G., Cheviron, B., Courault, D. and Charron, F.: Soil moisture retrieval over irrigated  
660 grassland using X-band SAR data, *Remote Sens. Environ.*, 176, 202–218, doi:10.1016/j.rse.2016.01.027, 2016.
- 661 El Hajj, M., Baghdadi, N., Bazzi, H. and Zribi, M.: Penetration Analysis of SAR Signals in the C and L Bands for Wheat, Maize, and  
662 Grasslands, *Remote Sens.*, 11(1), 22–24, doi:10.3390/rs11010031, 2019.
- 663 Holah, N., Baghdadi, N., Zribi, M., Bruand, A. and King, C.: Potential of ASAR/ENVISAT for the characterization of soil surface  
664 parameters over bare agricultural fields, *Remote Sens. Environ.*, 96(1), 78–86, doi:10.1016/j.rse.2005.01.008, 2005.
- 665 Hosseini, M. and McNairn, H.: Using multi-polarization C- and L-band synthetic aperture radar to estimate biomass and soil moisture of  
666 wheat fields, *Int. J. Appl. Earth Obs. Geoinf.*, 58, 50–64, doi:10.1016/j.jag.2017.01.006, 2017.
- 667 IPCC: Climate Change 2014: Synthesis Report. Contribution of Working Groups I, II and III to the Fifth Assessment Report of the  
668 Intergovernmental Panel on Climate Change [Core Writing Team, R.K. Pachauri and L.A. Meyer (eds.)], Geneva, Switzerland., 2014.
- 669 Jarlan, L., Khabba, S., Er-Raki, S., Le Page, M., Hanich, L., Fakir, Y., Merlin, O., Mangiarotti, S., Gascoin, S., Ezzahar, J., Kharrou, M.  
670 H., Berjamy, B., Saaïdi, A., Boudhar, A., Benkaddour, A., Laftouhi, N., Abaoui, J., Tavernier, A., Boulet, G., Simonneaux, V., Driouech,  
671 F., El Adnani, M., El Fazziki, A., Amenzou, N., Raïbi, F., El Mandour, H., Ibouh, H., Le Dantec, V., Habets, F., Trambly, Y., Mougnot,

- 672 B., Leblanc, M., El Faïz, M., Drapeau, L., Coudert, B., Hagolle, O., Filali, N., Belaqziz, S., Marchane, A., Szczypta, C., Toumi, J., Diarra,  
673 A., Aouade, G., Hajhouji, Y., Nassah, H., Bigeard, G., Chirouze, J., Boukhari, K., Abourida, A., Richard, B., Fanise, P., Kasbani, M.,  
674 Chakir, A., Zribi, M., Marah, H., Naimi, A., Mokssit, A., Kerr, Y. and Escadafal, R.: Remote Sensing of Water Resources in Semi- Arid  
675 Mediterranean Areas: the joint international laboratory TREMA, *Int. J. Remote Sens.*, 36(19–20), 4879–4917,  
676 doi:10.1080/01431161.2015.1093198, 2015.
- 677 Jarlan, L., Khabba, S., Szczypta, C., Lili-Chabaane, Z., Driouech, F., Le Page, M., Hanich, L., Fakir, Y., Boone, A. and Boulet, G.: Water  
678 resources in South Mediterranean catchments Assessing climatic drivers and impacts W ater resources, in *The Mediterranean Region*  
679 *under Climate Change*, Marseille., 2016.
- 680 Khabba, S., Duchemin, B., Hadria, R., Er-Raki, S., Ezzahar, J., Chehbouni, A., Lahrouni, A. and Hanich, L.: Evaluation of digital  
681 Hemispherical Photography and Plant Canopy Analyzer for Measuring Vegetation Area Index of Orange Orchards, *J. Agron.*, 8, 67–72,  
682 doi:10.3923/ja.2009.67.72, 2009.
- 683 Lee, C., Lu, Z. and Jung, H.: Simulation of time-series surface deformation to validate a multi- interferogram InSAR processing technique,  
684 *Int. J. Remote Sens.*, 33(22), 7075–7087, doi:10.1080/01431161.2012.700137, 2012.
- 685 Lenoble, J., Herman, M., Deuzé, J. L., Lafrance, B., Santer, R. and Tanré, D.: A successive order of scattering code for solving the vector  
686 equation of transfer in the earth’s atmosphere with aerosols, *J. Quant. Spectrosc. Radiat. Transf.*, 107(3), 479–507,  
687 doi:10.1016/j.jqsrt.2007.03.010, 2007.
- 688 Li, J. and Wang, S.: Using SAR-derived vegetation descriptors in a water cloud model to improve soil moisture retrieval, *Remote Sens.*,  
689 10(9), doi:10.3390/rs10091370, 2018.
- 690 Li, Y. Y., Zhao, K., Ren, J. H., Ding, Y. L. and Wu, L. L.: Analysis of the dielectric constant of saline-alkali soils and the effect on radar  
691 backscattering coefficient: A case study of soda alkaline saline soils in western Jilin province using RADARSAT-2 data, *Sci. World J.*, 1–  
692 14, doi:10.1155/2014/563015, 2014.
- 693 Major, D. G., Schaalje, G. B., Asrar, G. and Kanemasu, E. T.: Estimation Of Whole-Plant Biomass And Grain Yield From Spectral  
694 Reflectance Of Cereals, *Can. J. Remote Sens.*, 12(I), 47–54, 1986.
- 695 Mattia, F., Le Toan, T., Picard, G., Posa, F. I., D’Alessio, A., Notarnicola, C., Gatti, A. M., Rinaldi, M., Satalino, G. and Pasquariello, G.:  
696 Multitemporal C-band radar measurements on wheat fields, *IEEE Trans. Geosci. Remote Sens.*, 41(7 PART I), 1551–1560,  
697 doi:10.1109/TGRS.2003.813531, 2003.
- 698 *Ministre de l’agriculture et peche maritime du developement rurale et des eaux et forets*, Ed.: *Agriculture en chiffres 2017*, 2018th ed.,  
699 *PLAN MAROC VERT*. [online] Available from: <http://www.agriculture.gov.ma/sites/default/files/AgricultureEnChiffre2017VAVF.pdf>,  
700 2018.
- 701 *Mission, R. O. and Services, G. O.*: *ESA’s Radar Observatory Mission for GMES Operational Services*, SP-1322/1., 2012.
- 702 Morrison, K., Bennett, J. C., Nolan, M. and Menon, R.: Laboratory Measurement of the DInSAR Response to Spatiotemporal Variations  
703 in Soil Moisture - *IEEE Journals & Magazine*, *IEEE Trans. Geosci. Remote Sens.*, 49(10), 3815–3823, doi:10.1109/TGRS.2011.2132137,  
704 2011.
- 705 Nolin, M. ., Quenum, M., Cambouris, A. ., Martin, A. and Cluis, D.: Rugosité de la surface du sol – description et interprétation, *Agrisol*,  
706 16(1), 5–21, 2005.
- 707 Norman, J. M., Kustas, W. P. and Humes, K. S.: Source approach for estimating soil and vegetation energy fluxes in observations of  
708 directional radiometric surface temperature, *Agric. For. Meteorol.*, 77(3–4), 263–293, doi:10.1016/0168-1923(95)02265-Y, 1995.
- 709 Ouiaadi, N., Ezzahar, J., Khabba, S., Er-Raki, S., Chakir, A., Ait Hssaine, B., Le Dantec, V., Rafi, Z., Beaumont, Antoine; Kasbani, M. and  
710 Jarlan, L.: C-band radar data and in situ measurements for the monitoring of wheat crops in a semi-arid area (center of Morocco),  
711 *DataSuds*, [online] Available from: <https://doi.org/10.23708/8D6WQC>, 2020a.
- 712 Ouiaadi, N., Jarlan, L., Ezzahar, J., Zribi, M., Khabba, S., Bouras, E., Bousbih, S. and Frison, P.: Monitoring of wheat crops using the  
713 backscattering coefficient and the interferometric coherence derived from Sentinel-1 in semi-arid areas, *Remote Sens. Environ.*, 251(C),  
714 doi:10.1016/j.rse.2020.112050, 2020b.
- 715 Ouiaadi, N., Jarlan, L., Ezzahar, J., Zribi, M., Khabba, S., Bouras, E. and Frison, P.-L.: Surface Soil Moisture Retrieval Over Irrigated  
716 Wheat Crops in Semi-Arid Areas using Sentinel-1 Data, in *2020 IEEE Mediterranean and Middle-East Geoscience and Remote Sensing*  
717 *Symposium (M2GARSS)*, pp. 212–215., 2020c.

- 718 Ouadi, N., Jarlan, L., Ezzahar, J., Khabba, S., Dantec, V. Le, Rafi, Z., Zribi, M. and Frison, P.-L.: Water Stress Detection Over Irrigated  
719 Wheat Crops in Semi-Arid Areas using the Diurnal Differences of Sentinel-1 Backscatter, in 2020 IEEE Mediterranean and Middle-East  
720 Geoscience and Remote Sensing Symposium (M2GARSS), pp. 306–309., 2020d.
- 721 Patel, P., Srivastava, H. S. and Navalgund, R. R.: Estimating wheat yield: an approach for estimating number of grains using cross-  
722 polarised ENVISAT-1 ASAR data, *Microw. Remote Sens. Atmos. Environ.* V, 6410, 641009, doi:10.1117/12.693930, 2006.
- 723 Periasamy, S.: Significance of dual polarimetric synthetic aperture radar in biomass retrieval : An attempt on Sentinel-1, *Remote Sens.*  
724 *Environ.*, 217, 537–549, doi:10.1016/j.rse.2018.09.003, 2018.
- 725 Petcu, E., Petcu, G., Lazăr, C. and Vintilă, R.: Relationship between leaf area index, biomass and winter wheat yield obtained at fundulea,  
726 under conditions of 2001 year, *Rom. Agric. Res.*, 19–20, 21–29, 2003.
- 727 Picard, G., Toan, T. Le and Mattia, F.: Understanding C-Band Radar Backscatter From Wheat Canopy Using a Multiple-Scattering  
728 Coherent Model, *IEEE Trans. Geosci. Remote Sens.*, 41(7), 1583–1591, doi:10.1109/TGRS.2003.813353, 2003.
- 729 Rahman, H., Dedieu, G. and Rahmant, H.: SMAC: a simplified method for the atmospheric correction of satellite measurements in the  
730 solar spectrum, *INT. J. Remote Sens.*, 15(1), 123–143, doi:10.1080/01431169408954055, 1994.
- 731 Rodell, M., Houser, P. R., Jambor, U., Gottschalck, J., Mitchell, K., Memg, C.-J., Arsenault, K., Cosgrove, B., Radakovich, J., Bosilovich,  
732 M., Entin, J. K., Walker, J. P., Lohmann, D. and Toll, D.: The Global Land Data Assimilation System, *Bull. Am. Meteorol. Soc.*, 85(3),  
733 381–394, doi:10.1175/BAMS-85-3-381, 2004.
- 734 Sabater, J. M., Jarlan, L., Calvet, J.-C. and Bouyssel, F.: From Near-Surface to Root-Zone Soil Moisture Using Different, *J. Hydrol.*, 8,  
735 194–206, doi:10.1175/JHM571.1, 2006.
- 736 Santoro, M., Wegmüller, U. and Askne, J. I. H.: Signatures of ERS-Envisat interferometric SAR coherence and phase of short vegetation:  
737 An analysis in the case of maize fields, *IEEE Trans. Geosci. Remote Sens.*, 48(4), 1702–1713, doi:10.1109/TGRS.2009.2034257, 2010.
- 738 Scott, C. P., Lohman, R. B. and Jordan, T. E.: InSAR constraints on soil moisture evolution after the March 2015 extreme precipitation  
739 event in Chile, *Sci. Rep.*, 7(1), doi:10.1038/s41598-017-05123-4, 2017.
- 740 Small, D. and Schubert, A.: Guide to ASAR Geocoding, ESA-ESRIN Tech. Note RSL-ASAR-GC-AD, (1.01), 1–36, doi:RSL-ASAR-GC-  
741 AD, 2008.
- 742 Sure, A. and Dikshit, O.: Estimation of root zone soil moisture using passive microwave remote sensing: A case study for rice and wheat  
743 crops for three states in the Indo- Gangetic basin, *J. Environ. Manage.*, 234, 75–89, doi:10.1016/j.jenvman.2018.12.109, 2019.
- 744 Taconet, O., Benallegue, M., Vidal-Madjar, D., Prevot, L., Dechambre, M. and Normand, M.: Estimation of soil and crop parameters for  
745 wheat from airborne radar backscattering data in C and X bands, *Remote Sens. Environ.*, 50(3), 287–294, doi:10.1016/0034-  
746 4257(94)90078-7, 1994.
- 747 Torres, R., Snoeij, P., Geudtner, D., Bibby, D., Davidson, M., Attema, E., Potin, P., Rommen, B., Floury, N., Brown, M., Navas, I.,  
748 Deghaye, P., Duesmann, B., Rosich, B., Miranda, N., Bruno, C., Abbate, M. L., Croci, R., Pietropaolo, A., Huchler, M. and Rostan, F.:  
749 GMES Sentinel-1 mission, *Remote Sens. Environ.*, 120, 9–24, doi:10.1016/j.rse.2011.05.028, 2012.
- 750 Touzi, R., Lopes, A., Bruniquel, J. and Vachon, P. W.: Coherence estimation for SAR imagery, *IEEE Trans. Geosci. Remote Sens.*, 37(1  
751 PART 1), 135–149, doi:10.1109/36.739146, 1999.
- 752 Ulaby, F., Moore, R. and Fung, A.: Microwave remote sensing active and passive-volume III: from theory to applications. [online]  
753 Available from: <https://infoscience.epfl.ch/record/51983> (Accessed 10 August 2018), 1986.
- 754 Ulaby, F. T. and Batlivala, percy P.: Optimum Radar Parameters for Mapping Soil Moisture, *IEEE Trans. Geosci. Electron.*, GE-14(2),  
755 81–93, 1976.
- 756 Ulaby, F. T. and Dobson, M. C.: Microwave Soil Moisture Research, *IEEE Trans. Geosci. Remote Sens.*, GE-24(1), 23–36,  
757 doi:10.1109/TGRS.1986.289585, 1986.
- 758 Ulaby, F. T., Aslam, A. and Dobson, M. C.: Effects of Vegetation Cover on the Radar Sensitivity to Soil Moisture, *IEEE Trans. Geosci.*  
759 *Remote Sens.*, GE-20(4), 476–481, doi:10.1109/TGRS.1982.350413, 1982.
- 760 Veci, L.: Sentinel-1 Toolbox: TOPS Interferometry Tutorial. [online] Available from: <http://www.ggki.hu/~banyai/S1TBX/S1TBX>  
761 Stripmap Interferometry with Sentinel-1 Tutorial.pdf, 2015.

- 762 Veloso, A., Mermoz, S., Bouvet, A., Le Toan, T., Planells, M., Dejoux, J. F. and Ceschia, E.: Understanding the temporal behavior of  
763 crops using Sentinel-1 and Sentinel-2-like data for agricultural applications, *Remote Sens. Environ.*, 199, 415–426,  
764 doi:10.1016/j.rse.2017.07.015, 2017.
- 765 Wang, H., Magagi, R. and Goïta, K.: Potential of a two-component polarimetric decomposition at C-band for soil moisture retrieval over  
766 agricultural fields, *Remote Sens. Environ.*, 217, 38–51, doi:10.1016/j.rse.2018.08.003, 2018.
- 767 Wang, P., Song, X., Han, D., Zhang, Y. and Zhang, B.: Determination of evaporation, transpiration and deep percolation of summer corn  
768 and winter wheat after irrigation, *Agric. Water Manag.*, 105, 32–37, doi:10.1016/j.agwat.2011.12.024, 2012.
- 769 Wegmuller, U. and Werner, C.: Retrieval of Vegetation Parameters with SAR Interferometry, *IEEE Trans. Geosci. Remote Sens.*, 35(1),  
770 18–24, doi:10.1109/36.551930, 1997.
- 771 Zan, F. De and Guarnieri, A. M.: TOPSAR: Terrain Observation by Progressive Scans, *IEEE Trans. Geosci. Remote Sens.*, 44(9), 2352–  
772 2360, doi:10.1109/TGRS.2006.873853, 2006.
- 773 De Zan, F., Parizzi, A., Prats-Iraola, P. and López-dekker, P.: A SAR Interferometric Model for Soil Moisture, *IEEE Trans. Geosci.*  
774 *Remote Sens.*, 52(1), 418–425, 2014.
- 775 Zribi, M., Kotti, F., Amri, R., Wagner, W., Shabou, M., Lili-Chabaane, Z. and Baghdadi, N.: Soil moisture mapping in a semiarid region,  
776 based on ASAR/Wide Swath satellite data, *Water Resour. Res.*, doi:10.1002/2012WR013405, 2014.
- 777